Joint Centre for Mesoscale Meteorology, Reading, UK

Frontal wave stability during moist deformation frontogenesis.

Part 1. Linear wave dynamics.

A. J. Thorpe
C. H. Bishop

Internal Report No. 16

May 1993

Met Office Joint Centre for Mesoscale Meteorology Department of Meteorology
University of Reading PO Box 243 Reading RG6 6BB United Kingdom
Tel: +44 (0)118 931 8425 Fax: +44 (0)118 931 8791
www.metoffice.com

Frontal wave stability during moist deformation frontogenesis.

Part I. Linear wave dynamics.

Craig H. Bishop and Alan J. Thorpe

Department of Meteorology, University of Reading, England.

Abstract.

It has been shown that lower tropospheric potential vorticity zones formed during moist deformation frontogenesis will support growing waves if at some time the frontogenesis ceases. In this paper, we identify the ways in which these waves are affected by the frontogenetic process.

Observations show that fronts in the eastern Atlantic commonly feature saturated ascent regions characterized by zero *moist* potential vorticity. Furthermore, in many cases the horizontal temperature gradient in the lowest one to two kilometers of the atmosphere is rather weak. These features are incorporated in an analytical archetype. The dynamical implications of saturated ascent in conditions of zero moist potential vorticity are represented in the model by assuming that adiabatic temperature changes are precisely balanced by diabatic tendencies. The observed small temperature gradient at low levels is represented in the model by taking it to be zero in the lowest one to two kilometers. Consequently, the forcing of the low-level moist ageostrophic vortex stretching which strengthens the low-level potential vorticity anomaly is confined to mid and upper levels.

A semi-analytical initial value solution for the linear development of waves on the evolving low-level potential vorticity anomaly is obtained. The waves approximately satisfy the inviscid primitive equations whenever the divergent part of the perturbation is negligible relative to the rotational part. The range of non-modal wave developments supported by the front are summarised using *RT* phase diagrams. Our analysis shows that the most dramatic effects of frontogenesis on frontal wave growth are due to (a) the increase in time of the potential vorticity and hence potential instability of the flow and (b) the increase in time of the along front

wavelength relative to the width of the strip. An optimally growing streamfunction wave is described. Finally, a diagnostic technique suitable for identifying small amplitude frontal waves in observational data is described.

1. Introduction

A complete understanding of frontal instability must include stability analyses of developing fronts. Some progress toward this goal has been made by Joly and Thorpe (1991). They examined the growth of eigenvectors of the resolvent matrix for the linear tangent model of moist Eady waves of differing meridional wavelengths and were thus able to indicate the stability of moist Eady fronts (cf. Eady 1949). In the Eady model, frontogenesis is initiated by horizontal shearing of the basic state north-south temperature gradient. Whilst this mechanism is a component of frontogenesis, observations suggest that frontogenetic forcing is often dominated by the compression of the cross-front temperature gradient by horizontal deformation.

A mathematical model of frontogenesis produced by horizontal deformation is given by Hoskins and Bretherton (1972)[1]. As shown in Thorpe and Emanuel (1985; hereafter TE), when condensation processes are included in the deformation model the latent heat released by water vapor condensing in the frontal updraft produces a local, line symmetric extremum in potential vorticity (PV) at low-levels along the front. This PV anomaly satisfies the Charney and Stern (1962) necessary condition for internal instability. Indeed, Joly and Thorpe (1990) have shown that 1000 km

[1]For a discussion of the history of frontal wave studies the reader is referred to Joly and Thorpe (1990) and Joly and Thorpe (1991).

wavelength normal modes can grow on such fronts with e-folding times of about a day. However, their results only apply to fronts which are not subject to frontogenesis or frontolysis. Developing fronts must have vertical circulations and these are not included in Joly and Thorpe's (1990) model. The frontal wave model to be described in this paper includes such processes and allows their effects on growth to be isolated.

As shown by Bretherton (1966) and discussed more recently in § 6 of Hoskins et. al. (1985), instabilities in non-developing flows of the barotropic type arising from strips of anomalous PV such as those found at fronts, may be understood in terms of the synergistic interaction of counter-propagating Rossby edge waves. Consider what these concepts suggest about the stability of a front undergoing moist deformation frontogenesis.

Fig 1(a) shows PV strips with wave disturbances on one edge only and the wind vectors induced by such disturbances. It can be shown that the speed of such waves is proportional to the ratio of its wavelength over the width of the strip. Now suppose that edge waves were present on both sides of the vortex strip and that their wavelengths were such that the wave propagation speed was exactly half of the total wind shear across the PV anomaly. Then, as described in § 6 of Hoskins et al. (1985), all configurations not characterised by a quarter wavelength phase shift between eastern and western waves will adjust toward the configuration shown in Fig. 1(b). In this configuration, each wave makes the other grow. This is due to the fact that each wave induces a wind field at the other wave which advects its crests and troughs even further away from their equilibrium position.

Now consider what happens if the PV strip supporting such a wave is subject to a deformation wind field, $(u_d,v_d)=(-\alpha x,\alpha y)$ and the convergent

ageostrophic wind typical of surface fronts. Firstly, deformation and ageostrophic convergence both act to increase the wavelength of the wave relative to the (decreasing) width of the PV anomaly. When this happens the propagation speed of the edge waves becomes faster relative to the cross-front shear. This causes the waves to move into a configuration like that shown in Fig. 1(c). This effect is stabilising as, obviously, such a configuration allows less mutual amplification than that depicted in Fig. 1(b). Another stabilising effect of the cross-frontal convergence is that it reduces the wave amplitude by directly compressing the crests and troughs of any nascent wave. On the other hand, when the air is saturated, the vertical ageostrophic flow increases the PV of the strip (shown by darker stippling in Fig. 1(c)) which would, in isolation, facilitate wave growth. Thus, stabilising and destabilising effects compete as frontogenesis proceeds. Consequently, one of the primary aims of this paper is

(i) to precisely describe how typical frontogenetic flows affect the growth and behaviour of the edge waves of a PV strip.

To achieve this, we will utilise the "*RT*" phase diagrams developed in Bishop (1993a) to synthesize the infinite number of non-modal developments described by the semi-analytic solution. These diagrams depict the evolution of horizontal structure for a wide range of initial conditions. In the second part of this paper, we develop diagnostics based on a mathematical model of Bretherton's explanation of instability in terms of counterpropagating edge waves.

The plan of the paper is as follows. Based on observations from the Fronts 87 experiment, in § 2 we develop a simplified mathematical description of North Atlantic fronts. Equations governing the evolution of

waves on such fronts are developed and solved in § 3. Section 4 contains the major results of this paper including a description of the normal modes of various stationary states that the evolving front passes through, an analysis of the behaviour of the non-modal waves of the evolving system using *RT* phase diagrams, and a presentation of a diagnostic suitable for detecting small amplitude frontal waves on observed fronts. The paper concludes with a summary and discussion in § 5.

2. Idealised moist front.

Our primary aim was to construct a model of moist frontogenesis simple enough to enable the edge wave interactions on a PV anomaly subject to latent heat release and ageostrophic convergence to be handled analytically. As in any theoretical study not all aspects of a real front can be incorporated but the key elements essential to all moist deformation frontogenesis are included; i.e. a horizontal deformation field, a frontogenetic ageostrophic flow and latent heat release. A number of different arrangements were tried and the following is a description of the most realistic front for which analytic solutions were obtained.

Data from the Fronts 87 research experiment indicates that the low level temperature gradients at eastern north Atlantic fronts are often very small (cf. Fig. 2). This suggests that the behaviour of waves on the low-level PV strips observed in Fronts 87 might be similar to the behaviour of waves in a precisely barotropic low-level zone. We divided the low-level vorticity into discrete regions of uniform vorticity surmising that this would allow analytic techniques similar to those used by Rayleigh (1880), and Dritschel et al (1991) to be applied. The evolution equations for this structure were deduced from the following considerations.

(a) Dynamics.

Data examined by Emanuel (1983), Emanuel (1988) and Thorpe and Clough 1991, (hereafter TC), indicate that in winter, over the mid-latitude oceans, the moist potential vorticity (PV_e) of frontal regions is often nearly zero in the saturated ascent zones. When $PV_e=0$ the θ_e surfaces are parallel to the absolute momentum, M, surfaces; where, (taking the front to be parallel to the y-axis), $M= fx + v$, f, denoting Coriolis parameter and v, the along front wind. Furthermore, if the air is saturated then the lapse rate of potential temperature θ along the M-surfaces will be that of the corresponding moist adiabat. Consequently, if air is ascending in such regions, the diabatic heating will be such as to ensure that at any height the (virtual) potential temperature of rising air will be equal to that of the air in its immediate neighborhood. Thus, in such regions of the atmosphere, vertical motion has precisely zero impact on the mass field of the atmosphere. This thermodynamic characteristic of frontal ascent may be simply expressed by taking the diabatic heating, $\overline{E}$, to be related to the vertical velocity, $\overline{w}$ such that

$$\overline{E} = \overline{w}\left(\frac{\partial\overline{\theta}}{\partial z}\right)_M \qquad (2.1)$$

where the subscript M indicates that the vertical derivative is to be taken along M-surfaces. (The overbar is used to indicate that the evolving front described here is just the basic state for the frontal waves described in Section 3). The significance of (2.1) is that for a two-dimensional front in thermal wind balance, the thermodynamic equation reduces to the form:

$$\partial\bar{\theta}/\partial T - \alpha X\ \partial\bar{\theta}/\partial X + (\alpha Y + \overline{v}_g)\partial\bar{\theta}/\partial Y = 0. \qquad (2.2)$$

where $(X, Y, Z, T)=(x + (\overline{v}_g/f), y, z, t)$ are the familiar geostrophic coordinates. For a front in a background deformation flow of strength α, the coordinates $(X',Y',Z',T') = (X\exp(\alpha T), Y\exp(-\alpha T), Z, T)$ reduce (2.2) to the statement $\partial\bar{\theta}/\partial T'=0$. Thus, *any* time dependent $\bar{\theta}$ of the form

$$\bar{\theta}(X,Y,Z,T) = \bar{\theta}\left\{X\exp(\alpha T),\ Y\exp(-\alpha T),\ Z,\ 0\right\} \qquad (2.3)$$

will satisfy (2.2). Thus, wherever (2.1) applies, horizontal deformation produces a simple compression of the isotherms.

Eq. (2.1) is a good approximation of latent heat release, only where the air is saturated and the equivalent potential temperature, θ_e, and M surfaces are almost parallel. To construct such a basic state, we took $\bar{\theta}$ to be equal to a basic state stratification $\theta(Z)$ equal to the lapse rate along a moist adiabat, plus a perturbation $\bar{\theta}'$. The moist adiabat chosen as a reference state was that for the wet bulb potential temperature equal to 12^0 C . Saturated descent is only realistic immediately beneath the front but for the sake of mathematical simplicity we assume all descent is saturated. (As is shown later, the error associated with the neglect of the adiabatic heating of descent, being proportional to the descent rate, can be significantly reduced by constructing fronts with very slow descent rates).

To relate the along front flow, $\bar{v}_g$, to $\partial\bar{\theta}'/\partial X$ using the thermal wind relation, we must first determine the temporal variation of $\bar{v}_g$ at some height. This depends on what effect the coriolis torque on the cross-front horizontal ageostrophic wind $\bar{u}_a$ has on the along front wind. Defining an ageostrophic streamfunction for the basic state, $\bar{\psi}$, such that $(\bar{u}_a, \bar{w}) = (\bar{\psi}_Z, -\bar{\psi}_X)$, Hoskins and Bretherton (1972) give its governing equation as

$$f^2\frac{\partial^2\bar{\psi}}{\partial Z^2} + \frac{g}{f\theta_0}\frac{\partial}{\partial X}\left(\bar{q}\frac{\partial\bar{\psi}}{\partial X}\right) = -2\alpha\left(\frac{g}{\theta_0}\right)\frac{\partial\bar{\theta}'}{\partial X} - \left(\frac{g}{\theta_0}\right)\frac{\partial\bar{E}}{\partial X},$$

with $\bar{\psi} = 0$ at the upper and lower frictionless boundaries; here, $\bar{q}$ denotes the dry potential vorticity equal; *i.e.* $\bar{q} = \left(f + \partial\bar{v}_g/\partial x\right)\left(\partial\bar{\theta}/\partial z\right)_M$. g denotes the gravitational constant and θ_0, a constant reference potential

temperature. Noting that $f\overline{w} = \left(f + \partial\overline{v}_g/\partial x\right)\left(\partial\overline{\psi}/\partial X\right)$ and substituting from (2.1), yields the simple form

$$\frac{\partial^2\overline{\psi}}{\partial Z^2} = -\frac{2\alpha}{f^2}\left(\frac{g}{\theta_0}\right)\frac{\partial\overline{\theta}'}{\partial X}. \tag{2.4}$$

Choosing $\overline{\theta}'$ to be a separable function in the deforming coordinates X' and Z', i.e. letting

$$g\overline{\theta}'/\theta_0 = F(Z')\left(B(X') - B_0\right), \tag{2.5}$$

where B_0 is some constant reference value, means that the solution to (2.4) will also be a separable function of X' and Z'. Consequently, there will be some height Z_c at which $\partial\overline{\psi}/\partial Z = 0$. With $\partial\overline{\psi}/\partial Z = 0$, the along front momentum equation, (cf. Hoskins and Bretherton 1972), requires that $\partial\overline{v}_g/\partial T' = -\alpha\overline{v}_g$ and hence that

$$\overline{v}_g(X, Z_c, T) = \overline{v}_g(X', Z_c, 0)\, e^{-\alpha T'}.$$

Following Hoskins and Bretherton (1972), we assume that the front grew via deformation from a quiescent ($\overline{v}_g$=0) state with vanishingly small temperature gradients. With this assumption, the above equation dictates that $\overline{v}_g$ will be zero at the height Z_c for all time. Having defined $\overline{v}_g$ to be zero at the reference level Z_c, it is now a simple matter to integrate $(g/f\theta_0)\partial\overline{\theta}'/\partial X$ to obtain $\overline{v}_g(X, Z, T)$.

In Appendix A we show that whilst the assumption of cross-front geostrophic balance is accurate in the barotropic layer for all strain rates and all frontal intensities, the neglect of cross-frontal accelerations above the barotropic layer can lead to serious errors when the vorticity of the front becomes large. For α/f equal 0.1 and 0.02 such serious errors will occur when the absolute vorticity of the frontal vortex reaches $6f$ and $17f$, respectively. These limitations should be kept in mind when attempting to relate the specific results of this paper to the stability of observed fronts.

(b) Structure of idealised front.

As mentioned previously, the aim was to construct a simple front with a low-level barotropic zone featuring discrete regions of uniform vorticity. Eq.(2.5) shows that the thermal structure of the front is defined by the functions F, B and B_0.

The low-level baroclinicity was incorporated simply by choosing F so that it was zero below some height Z_B and sinusoidal above. The discrete regions of uniform vorticity were achieved by letting B be a quadratic function of X' in such regions. As a major aim is to study the interaction of edge waves propagating on the gradients between such regions, we also define transition regions in which the vorticity varies smoothly from one constant to another. In these regions B is a cubic function of X'.

In order to obtain a realistic frontal structure, we define 7 distinct horizontal regions. These regions are illustrated in Fig. 3a, which depicts the $\overline{\theta}'$ and vorticity structure of an idealised occluded front in geostrophic coordinates. As is evident from Fig. 3(a), the seven regions were joined together by requiring that both $\overline{\theta}'$ and $\partial\overline{\theta}'/\partial X'$ be continuous across the boundaries of the regions. Apart from the boundaries between, regions 1 and 2 and 6 and 7, we also require that $\partial^2\overline{\theta}'/\partial X'^2$ be continuous across boundaries.

Regions 1 and 7 represent the atmosphere far distant from the front for which the horizontal temperature gradients are zero. Region 2 is defined to be cold frontal as $\partial B/\partial X$ is positive and increases linearly with X. Region 6 is analogous to Region 4 but here $\partial\theta/\partial X$ is warm frontal and the magnitude of $\partial B/\partial X$ (here negative) decreases linearly with X. The variation of B with X produces anticyclonic-low-level vorticity in these regions. In the transition regions 3 and 5, $\partial B/\partial X$ varies quadratically with X so as to

ensure that the vorticity varies smoothly between regions 2, 4 and 6. In region 4, $\partial B/\partial X$ decreases linearly with X, thus producing positive vorticity at low-levels. The widths of the regions are chosen so that the magnitude of the positive vorticity is much greater than the magnitude of the anticyclonic vorticity.

As shown in Appendix B, it is a simple matter to give the occluded front an asymmetry such that the cold front is stronger than the warm front or *vice-versa*. The structure of a case where the cold front is stronger than the warm front is shown in Fig. 3b.

The stability analysis described in this paper is applicable to fronts of the form described above when the transition regions 3 and 5 are taken to be much narrower than region 4. Cross-sections of such fronts are displayed in cartesian space in Fig. 4. We present Fig. 4, to show the extent to which these fronts resemble the data from the Fronts 87 experiment. Qualitatively, the fields displayed in Fig's 4(a)-(d) bear a close resemblance to the corresponding fields displayed in TC. In 4(a), note the low-level PV anomaly - the source of wave growth in this model. Fig. 4(b) shows how the temperature gradient is confined to upper levels.

As discussed, eq. (2.1) is consistent with thermodynamic laws only for a saturated atmosphere having $\overline{PV}_e = 0$; i.e. where the M and $\bar{\theta}_e$ contours are parallel. Fig's 4(c),(d), (g) and (h) show the extent to which this condition is met by the idealised fronts. In the updraft regions of both fronts, the M and $\bar{\theta}_e$ surfaces are approximately parallel. In the descent regions, (2 and 6), the M and $\bar{\theta}_e$ surfaces become less parallel and in the lower part of the atmosphere $\partial\bar{\theta}_e/\partial z < 0$. It is assumed that the descent in these regions is sufficient to prevent the outbreak of convective cells. Referring to Fig. 2 of TC shows that this aspect of the models $\bar{\theta}_e$ profile

is realistic and was typical of the profiles observed in Fronts 87.

Note that the occluded front is nearer to moist neutrality than the cold front. Note also how reminiscent the kink in the streamfunction shown in Fig's 4(d) and (h) is to that obtained from the moist-up/dry-down simulations of both Emanuel (1985) and TE.

For the purposes of the stability studies in the remainder of this paper we assume that the relative vorticity of all fronts considered at t = 0 is equal to f. Thus, the constant defined by $\exp(-2\alpha T)\partial\bar{v}_g/\partial X = 0.5$ and consequently the vorticity in region 4 becomes infinite at the non-dimensional time αt_c, where

$$\alpha t_c = \frac{1}{2}\ln(2) = 0.347; \tag{2.6}$$

i.e. t_c = 9.63 hr/(αx10^5s). Fig's 3 and 4, however, pertain to the time T' = 4 hr/(αx10^5s); thus, they represent the front nearly halfway through the time it takes to form a discontinuity. To compute the ageostrophic streamfunction shown in Fig's 4(d) and (h), we assumed $\alpha = 10^{-5}s^{-1}$.

3. Analytic description of frontal waves

(a) Principal equations.

In this Section, we develop and solve equations for the perturbation horizontal wind field in the lowest 2 km. As shown in Part 2, these solutions implicitly describe the interaction of counterpropagating edge waves on a thinning, intensifying PV strip. As such the solution fulfills the aims of this paper. Some arguments to support the idea that a solution which ignores the interaction of the flow below and above 2 km can still capture the most important features of a complete solution are given in the concluding discussion.

Below $Z = Z_B$, all components of the basic state wind are independent

of height except w which varies linearly with height in the vortex bands. Assuming that vertical variations of the perturbation are negligible in this region, the unapproximated inviscid vorticity equation requires that

$$\frac{D}{Dt}\left(f + \frac{\partial^2\Psi}{\partial x^2} + \frac{\partial^2\Psi}{\partial y^2}\right) = \frac{\partial w}{\partial z}\left(f + \frac{\partial^2\Psi}{\partial x^2} + \frac{\partial^2\Psi}{\partial y^2}\right). \qquad (3.1)$$

where Ψ is the streamfunction for the non-divergent (rotational) horizontal wind, (u_r, v_r); i.e. $(-\partial\Psi/\partial y, \partial\Psi/\partial x) = (u_r, v_r)$ and $w = \overline{w} + w'$. The corresponding semi-geostrophic vorticity equation may be recovered by replacing the terms in brackets by their geostrophic counterparts. For the sake of a more accurate description of the flow we have chosen to use the (primitive) vorticity equation for this analysis.

Now let

$$\Psi = \alpha xy + \overline{\Psi}_g + \Psi' \text{ and the total flow } (u, v)=(-\alpha x + \overline{u}_a + u', \alpha y + \overline{v}_g + v'), \qquad (3.2)$$

where primed variables denote perturbations to the basic state and $\partial\overline{\Psi}_g/\partial x = \overline{v}_g$; then, using (3.2) in (3.1) and linearising leads to

$$\left[\frac{\partial}{\partial t} + (-\alpha x + \overline{u}_a)\frac{\partial}{\partial x} + (\alpha y + \overline{v}_g)\frac{\partial}{\partial y}\right]\zeta' + u'\frac{\partial\overline{\zeta}}{\partial x} = \zeta'\frac{\partial\overline{w}}{\partial z} \qquad (3.3)$$

where $\overline{\zeta} = f + \partial\overline{v}_g/\partial x$ is the absolute vorticity of the basic state, $u' = (u', v')$ and $\zeta' = (\partial^2\Psi'/\partial x^2 + \partial^2\Psi'/\partial y^2)$.

The x and y dependent coefficients may be removed from the Lagrangian operator in (3.3) by using the (X', Y', Z', T') coordinates introduced earlier. The vorticity equation becomes

$$\left[\frac{\partial}{\partial T'} + \overline{v}_g(X', T')e^{-\alpha T'}\frac{\partial}{\partial Y'}\right]\zeta' + u'e^{\alpha T'}\frac{\overline{\zeta}}{f}\frac{\partial\overline{\zeta}}{\partial X'} = \zeta'\frac{\partial\overline{w}}{\partial Z'}, \qquad (3.4)$$

In regions of uniform vorticity, $\zeta' = 0$ is an exact solution to (3.4). Within the transition regions, the perturbation wind fields create, via the $u'\partial\overline{\zeta}/\partial x$ term, non-zero ζ' - which is subsequently stretched or contracted by $\partial\overline{w}/\partial Z'$.

(b) Solution procedure.

In the following, we show how (3.4) can be solved by (a) utilising a symmetry associated with the vorticity equation for the basic state to absorb the perturbation vortex stretching term on the right hand side of (3.4), (b) letting the width of the transition regions be small enough to satisfy various constraints mentioned below, (c) integrating the equation across the transition regions, (d) finding the relationship between integrated quantities and the perturbation streamfunction, (e) requiring that the streamfunction be continuous across region boundaries and finally (f) utilising the R parameter technique introduced by Bishop (1993a) to define the implicitly non-modal solutions of the resulting equation.

Making the substitution

$$Q' = (f/\bar{\zeta})\zeta' \tag{3.5}$$

in (3.4), and using the fact that in the barotropic layer

$$D\bar{\zeta}/DT' = \left[\frac{\partial}{\partial \bar{T}'} + \bar{v}(X',T')e^{-\alpha T'}\frac{\partial}{\partial \bar{Y}'}\right]\bar{\zeta} = \bar{\zeta}\,\partial\bar{w}/\partial Z'$$

yields

$$\left[\frac{\partial}{\partial \bar{T}'} + \bar{v}(X',T')e^{-\alpha T'}\frac{\partial}{\partial \bar{Y}'}\right]Q' + u'e^{\alpha T'}\frac{\partial \bar{\zeta}}{\partial \bar{X}'} = 0. \tag{3.6}$$

The authors found the substitution (3.5) to be crucially important in solving (3.4).

Taking δL, the width of the transition regions in deforming geostrophic coordinates, to be small enough so as to enable the variations in $\bar{v}_g$ and u' across the transition regions to be ignored, it is a simple matter to integrate (3.6) across the transition regions to obtain

$$\left[\frac{\partial}{\partial \bar{T}'} + \bar{v}_{gJ}e^{-\alpha t}\frac{\partial}{\partial \bar{Y}'}\right]\tilde{Q}_J + u'e^{\alpha T'}\delta\bar{\zeta}_J = 0$$

where J stands for either 3 or 5 depending on the transition region being considered. The $\tilde{Q}_J$ are defined by

$$\tilde{Q}_3 = \int_{-\frac{L}{2}-\delta L}^{-\frac{L}{2}} Q'(X', Y', T')dX' \text{ and } \tilde{Q}_5 = \int_{\frac{L}{2}}^{\frac{L}{2}+\delta L} Q'(X', Y', T')dX'.$$

The net changes in absolute vorticities across the regions are $\delta\bar{\zeta}_3 = \bar{\zeta}_4 - \bar{\zeta}_2$ and $\delta\bar{\zeta}_5 = \bar{\zeta}_6 - \bar{\zeta}_4$ and the $\bar{v}_{gJ}$ are $\bar{v}_{g3} = \bar{v}_g(-\frac{L}{2}, T')$ and $\bar{v}_{g5} = \bar{v}_g(\frac{L}{2}, T')$. Assuming the non-divergent part of the wind remains much larger than the irrotational part u' may be replaced by its non-divergent part so that

$$\left[\frac{\partial}{\partial T'} + \bar{v}_{gJ}e^{-\alpha t}\frac{\partial}{\partial Y'}\right]\tilde{Q}_J - \Psi'_{Y'}\delta\bar{\zeta}_J = 0 \qquad (3.7)$$

In Appendix C, we show that the $\tilde{Q}_J$ and Ψ' are related according to

$$\tilde{Q}_3 = \left(v'_r(-\frac{L}{2}) - v'_r(-\frac{L}{2} - \delta L)\right)e^{\alpha T'} \text{ and } \tilde{Q}_5 = \left(v'_r(\frac{L}{2} + \delta L) - v'_r(\frac{L}{2})\right)e^{\alpha T'}; \qquad (3.8)$$

where $v'_r = \partial\Psi'/\partial x$ i.e. $e^{-\alpha T'}\tilde{Q}_J$ (J = 3 or 5) equals the change in the rotational part of the perturbation along front velocity across the relevant transition region. Eq. (3.8) enables the $\tilde{Q}_J$ and hence (3.7) to be expressed purely in terms of derivatives of Ψ'.

We now discuss the conditions that Ψ' itself must satisfy. Firstly, we need to ensure that the $\zeta' = 0$ condition is satisfied outside the transition regions. Secondly, as δL tends to zero the change in Ψ' across regions 3 and 5 must tend to zero. Finally, the amplitude of the streamfunction induced by edge waves must monotonically decrease with distance away from the front. To see that the chosen form of Ψ' satisfies these constraints, it is convenient to first describe it in terms of cartesian coordinates. Centering these coordinates so that the west and east edges of the strip lie at $-L_c/2$ and $L_c/2$, respectively, and letting Ψ'_2, Ψ'_4 and Ψ'_6 denote Ψ' in regions 2, 4 and 6, respectively. In regions 2 and 6, we take

$$\Psi'_2(x, y, t) = G(-L_c/2, t)\exp\left[l\left(\frac{L_c}{2} + x\right)\right]\exp\left[il\left(y - p'(t)e^{-\alpha t}\right)\right] \qquad (3.9a)$$

$$\Psi'_6(x,\ y,\ t) = G(L_c/2,\ t)\exp\left[il\left(\frac{L_c}{2} - x\right)\right]\exp\left[il\left(y - p'(t)e^{-\alpha t}\right)\right] \qquad (3.9b)$$

where l, the wavenumber, is real and $p'(t)$ is a complex function playing the role of an integrated complex phase speed in deforming coordinates. The $G(x,\ t)$ function, referred to in (3.9a) and (3.9b) defines the horizontal structure of Ψ' in region 4:

$$G(x,\ t) = C\ \exp\left(-lL_c/2\right)\left[lR(t)\sinh\left(lx\right) + \cosh\left(lx\right)\right] \qquad (3.9c)$$

and

$$\Psi'_4(x,\ y,\ t) = G(x,\ t)\ \exp\left[il\left(y - p'(t)e^{-\alpha t}\right)\right]. \qquad (3.9d)$$

In (3.9c), C is a complex constant defining the initial phase and amplitude of the wave and $R(t)$ is a complex function defining the evolution of the horizontal structure of the wave. Clearly, x and t are taken to be non-separable and consequently, in the terminology of Farrell (1984), our approach includes non-modal solutions.

Note that in regions 2 and 6, Ψ' attenuates with an e-folding distance of $\lambda/2\pi$, where λ is the along front wavelength. As can be shown from the results of the stability analyses presented later, the maximum wavelengths reached by the fastest growing waves which achieve amplifications greater than e are all less than 900 km. The minimum width of region 2 for our cold frontal case is 1026 km. Since a 900 km wavelength would attenuate more than 1000 times across such a distance and since the vorticity jumps at these outer edges are always less than a fifth of the size of the vorticity jumps across regions 3 and 5, it is clear that the outer edges have a negligible influence on the dynamics of waves on the main frontal vortex.

We now express the $\tilde{Q}_j$'s in terms of the expressions for Ψ'. Transforming (3.9) to (X',Y',Z',T') coordinates, letting δL tend to zero and applying (3.8) yields

$$\tilde{Q}_3 = Cl_0[lR(T') - 1]\exp\left\{il_0\left[Y' - p'(T')\right]\right\}, \tag{3.10a}$$

and

$$\tilde{Q}_5 = Cl_0[-lR(T') - 1]\exp\left\{il_0\left[Y' - p'(T')\right]\right\}, \tag{3.10b}$$

where $l_0 = l\exp(\alpha T')$. The significance of the R parameter can now be seen. The phase shift southward, $\Delta\chi$, of the edge wave in region 5 relative to that in region 3 is

$$\Delta\chi(T') = \arg^*[-lR(T') - 1] - \arg^*[lR(T') - 1]. \tag{3.11}$$

where $\arg^*$ is precisely defined in Appendix D but essentially stands for the argument of a complex variable; (Note that this argument must be defined in a way that ensures the continuity of the phase shift southward of a particular crest). It can be shown that if $R = (R_r, R_i)$, then $\Delta\chi$ has the same sign as R_r. When $\Delta\chi$ is positive, the vorticity wave leans against the shear and draws energy from it, whereas when $\Delta\chi$ is negative, the amplitude of the wave decays. The ratio of the amplitudes of the vorticity wave in region 5 to that in region 3, $\Delta|Q|$, is also determined by R, *viz.*

$$|\tilde{Q}_5|/|\tilde{Q}_3| = \frac{|(R_i - 1, R_r)|}{|(R_i + 1, R_r)|}. \tag{3.12}$$

Eq's (3.11) and (3.12) show that the horizontal structure of a frontal wave may be deduced by its R value on the complex plane.

We now show how the time rate of change of p' and R may be deduced from (3.7). Firstly, note that in deforming geostrophic coordinates

$$G(X',T') = C\exp\left[-\left(\frac{\dot{l}L}{2}\right)\right]\left[lR\sinh(\dot{l}X') + \cosh(\dot{l}X')\right] \tag{3.13a}$$

and where

$$\dot{l} = l_0 e^{-2\alpha T'}(f/\bar{\zeta}_4), \tag{3.13b}$$

where $\bar{\zeta}_4$ denotes the absolute vorticity in region 4. Eq. (3.7) could be solved at this point using substitutions from (3.13) and (3.10); however, the algebra is simplified considerably if one first writes $\bar{v}_{gJ}$ and $\delta\bar{\zeta}_J$ in

terms of their symmetric and asymmetric parts about $X' = 0$; i.e. we let

$$\bar{v}_{g3} = \left(\bar{v}_s - \bar{v}_n\right)e^{\alpha T'} \text{ and } \bar{v}_{g5} = \left(\bar{v}_s + \bar{v}_n\right)e^{\alpha T'} \tag{3.14a}$$

where

$$\bar{v}_s = -0.4\,\frac{H}{f}\,\Gamma \text{ and } \bar{v}_n = 0.4\,\frac{H}{f}\,\Lambda \tag{3.14b}$$

where Γ and Λ define the symmetric and antisymmetric parts of the temperature gradient; (cf. Appendix B, for details). Furthermore, we define

$$\delta\bar{\zeta}_3 = \delta\bar{\zeta}_n + \delta\bar{\zeta}_s \text{ and } \delta\bar{\zeta}_5 = -\delta\bar{\zeta}_n + \delta\bar{\zeta}_s, \tag{3.15a}$$

where

$$\delta\bar{\zeta}_n = \bar{\zeta}_4 - \frac{1}{2}\left(\bar{\zeta}_6 + \bar{\zeta}_2\right) \text{ and } \delta\bar{\zeta}_s = \frac{1}{2}\left(\bar{\zeta}_6 - \bar{\zeta}_2\right). \tag{3.15b}$$

Using (3.10) and (3.13)-(3.15) in (3.7), one can show that

$$-il_0\left[\left(\frac{dp'}{dT'}\right) - \bar{v}_s\right] = R\,\delta\bar{\zeta}_n\left(\frac{l_0\bar{v}_n}{\delta\bar{\zeta}_n} - e^{-\mu}\sinh(\mu)\right) - i\,\delta\bar{\zeta}_s e^{-\mu}\cosh(\mu) \tag{3.16}$$

$$\frac{dR}{dT'} = -\delta\bar{\zeta}_n\left[R^2\left(\frac{l_0\bar{v}_n}{\delta\bar{\zeta}_n} - e^{-\mu}\sinh(\mu)\right) + \left(\frac{l_0\bar{v}_n}{\delta\bar{\zeta}_n} - e^{-\mu}\cosh(\mu)\right)\right] + iR\,\delta\bar{\zeta}_s e^{-2\mu} \tag{3.17}$$

where $\mu = \dot{l}L/2$. Eq. (3.17) describes the relationship between the current horizontal structure of the wave (i.e. its R value) and its structural evolution, dR/dT'. Eq. (3.16) gives the relationship between the horizontal structure of a wave and its complex phase speed in deforming geostrophic coordinates at $X' = 0$.

Note that since

$$v_n \cong e^{-2\alpha T'}\,\frac{\partial\bar{v}_{g4}}{\partial X}\,\frac{L}{2}, \text{ when } \delta\bar{\zeta} \cong \frac{\partial\bar{v}_{g4}}{\partial x} = \frac{\bar{\zeta}_4}{f}\,\frac{\partial\bar{v}_{g4}}{\partial X}, \text{ it follows that}$$

$$\frac{l_0\bar{v}_s}{\delta\bar{\zeta}_n} = \mu. \tag{3.18}$$

Also note that since the along front wavelength $l = l_0 e^{-\alpha T'}$, and since the width, L_c, of region 4 in Cartesian space is given by $L_c = Le^{-\alpha T'} f/\bar{\zeta}$, it follows that μ is equal to the product of half the width of the vortex strip and the along front wavenumber. When these considerations are taken

into account it is readily seen that for α=0, (3.16) and (3.17) reduce to the non-modal form of Rayleigh's classical barotropic instability solution.

Throughout this set of papers eq's (3.16) and (3.17), which describe wave evolution on the basic state, were solved where necessary using a standard fourth order Runge-Kutta numerical algorithm.

4. Description of wave solutions.

(a) Normal modes ?

For α=0, the above system has amplifying normal modes, the growth rate and phase speed of these normal modes are recovered by letting R be equal to R_{nm} where R_{nm} is the positive value of R that makes $dR/dT' = 0$ and then substituting this value of R into (3.16) to recover the growth rate and phase speed.

Fig. 5a shows the variation of normal mode growth rate with 2μ for the cold front at several different stages of its development here identified by the non-dimensional time T_n where $T_n = T'/t_c$. Note that the exponential growth rates at $T_n = 0.8$ are an order of magnitude greater than those supported at $T_n = 0.0$. Note also that the high and low wavenumber cut offs for normal mode instability decrease as T_n increases. (We do not show the corresponding diagram for the occluded front as it is almost identical to Fig. 5a).

These normal mode growth rate curves could be used to measure the growth of a wave on a developing front if it could maintain a normal mode structure. As indicated by Fig. 5b, the 2μ value of waves on developing fronts decreases monotonically to zero at $T_n = 1$. Thus, a wave which maintained normal mode structure with an initial wavenumber, $2\mu_0$, equal to 2.1 would grow at the rate indicated by the dashed line on Fig. 5a.

Eq. (3.17), however, dictates that normal mode structure can only be

maintained for an instant in a developing flow. This is easily shown. As μ changes, R_{nm} changes; consequently, for R to remain equal to R_{nm}, dR/dT' must be non-zero, but *a priori* $dR/dT' = 0$ at $R = R_{nm}$. Thus, $d\mu/dt \neq 0 \Rightarrow$ no normal modes.

(b) RT phase diagrams.

As shown in Bishop (1993a), the R values that yield normal mode structures at any particular wavenumber play key roles in *RT* phase diagrams. These diagrams allow the qualitative nature of a wide range of non-modal developments to be seen at a glance. Briefly, the idea of an *RT* phase diagram is to overlay contours of the countershear phase shift, $\Delta\chi$, and the amplitude ratio of edge waves, $|\tilde{Q}_5|/|\tilde{Q}_3|$, on the complex R plane with the field of $(dR_r/dT', dR_i/dT')$ vectors implied by (3.17), where R_r and R_i are the real and imaginary parts of R, respectively. We call these vectors *RT* vectors. The diagrams enable changes in R to be easily related to changes in structure. In so doing they provide a method of qualitatively estimating the structural development of a wide range of initial structures. For example, with $2\mu = 2.1$ at $T_n = 0$, the *RT* phase diagram is as shown in Fig. 6a. At this value of 2μ the *RT* vectors simply circle around R_{nm}. This circling reflects the fact that at this wavenumber it is impossible for eastern and western edge waves to lock onto each other and that the region 5 edge wave would be continually advected north of the region 3 edge wave if 2μ were not monotonically decreasing with time.

Since 2μ does decrease, (3.17) dictates that the real part of R_{nm} eventually becomes greater than zero. When this happens the associated normal mode can amplify and the corresponding *RT* diagram radically changes its character, most importantly the *RT* vectors no longer circle around R_{nm} but rather converge towards it. This is illustrated by Fig. 6b which shows

the RT phase diagram for waves at $T_n = 0.4$ with $2\mu = 1.1$ and $R_{nm} = (0.95, 0.064)$. Note that all waves with $2\mu = 1.1$ at $T_n = 0.4$ correspond to waves which had $2\mu = 2.1$ at $T_n = 0$.

For the cold front, the imaginary parts of R_{nm} are always slightly positive for $\mathcal{R}e(R_{nm}) > 0$, whereas for the occluded front $Im(R_{nm})$ is zero whenever $\mathcal{R}e(R_{nm}) > 0$. This indicates that for the cold front, all non-modal waves having wavenumbers less than the high wavenumber cut off for normal mode instability tend towards a structure in which the amplitude of the wave in region 3 is slightly larger than that in region 5. This is a consequence of the fact that the vorticity jump across region 3 is greater than that across region 5 for the cold front. For the occluded front no such asymmetries are present and the R_{nm} values corresponding to low wavenumbers have zero imaginary part. Otherwise, the dependence on T_n of the R_{nm} values and RT diagrams pertaining to the occluded front is very similar to that for the cold front. From (3.16) and (3.17) it can be seen that this is a direct consequence of the fact that the ratio, $\delta\bar{\zeta}_s/\delta\bar{\zeta}_n$ is initially small and subsequently decreases to zero as T_n tends to infinity. Because of this there should be no qualitative differences between the stability of the occluded and warm fronts and only small quantitative differences. Consequently, for the remainder of this set of papers we shall focus on the stability of the structurally simpler occluded front and assume that its stability characteristics pertain, in a qualitative way at least, to the cold front.

An excellent indicator of non-modal wave growth is the counter-shear phase shift, $\Delta\chi$. Indeed, in Part 2 of this work we show that the growth of an edge wave is proportional to $\sin(\Delta\chi)$ multiplied by the ratio of the amplitude of the edge wave on the opposing boundary over the amplitude of

the edge wave whose growth is being considered. The temporal development of these quantities is described by *RT* phase diagrams. Thus, these results from the second part of this paper may be used in conjunction with *RT* diagrams to make qualitative predictions about edge wave growth.

Fig. 7 shows the variation of $\Delta\chi$ with T_n for wave disturbances with $2\mu = 2.1$ and $R = (122, 0)$ at $T_n = 0$. For the occluded front, (3.17) implies that dR_1/dT' is always equal to zero and hence if R is initially real, as it is for the current cases, it remains real for all time. For such waves the amplitudes of the waves in regions 3 and 5 remain equal for all time and hence horizontal structure and growth are uniquely defined by $\Delta\chi$ which in this case relates to R via the eq., $\Delta\chi = 2\tan^{-1}(R)$.

The *RT* diagrams indicate that when the $\mathcal{R}e\{R_{nm}\}$ is greater than zero, the R values of all non-modal[2] waves are attracted to R_{nm}. Consequently, the countershear phase shifts of all non-modal waves will be attracted to $\Delta\chi_{nm}$, the countershear phase shift of the normal mode of the instantaneous structure. This is essentially what is being seen in Fig. 7. For $\alpha = 0.2\times10^{-5}s^{-1}$, there is a relatively long period before the $\mathcal{R}e\{R_{nm}\}$ becomes greater than zero and before this time the phase shift almost reduces to zero. Before it does so $\mathcal{R}e\{R_{nm}\}$ becomes positive and thereafter it is attracted to ever increasing values of $\Delta\chi_{nm}$. Similar comments could be made about the structural development of waves on more highly strained fronts. As indicated by Fig. 7, however, the higher the strain rate the

[2]In reference to the work of Farrell (1984), a distinction needs to be drawn between his definition of non-modality (*viz.* non-modality ≡ non-separability of time) and the continuous spectrum of Pedlosky (1964). For the Eady (1949) problem the continuous spectrum is uniquely associated with non-uniformities in perturbation quasi-geostrophic PV; its counterpart for the current problem would be uniquely linked to non-uniformities in the perturbation vorticity field in regions 2, 4 or 6.

less closely the $\Delta\chi$ value of waves follow $\Delta\chi_{nm}$. This effect is because whilst $\Delta\chi_{nm}$ changes more rapidly as the strain rate is increased, the magnitude of the *RT* vector field at any time T_n is unaffected by the strain rate as the *RT* vectors depend only on the current non-dimensional wavelength and wind shear. Thus, $\Delta\chi$ tends to lag $\Delta\chi_{nm}$ by a greater amount at large strain rates simply because $\Delta\chi_{nm}$ moves faster at large strain rates.

As mentioned previously, edge wave growth is proportional to $\sin(\Delta\chi)$, thus, one might expect that the fastest growing waves will have initial $\Delta\chi$ values which maximize the amount of time the edge waves spend with a countershear phase shift of 90^0. For the set of waves shown in Fig. 7, it is apparent that the initial 179^0 phase shift is quite well suited for this for $\alpha = 0.2\times10^{-5}s^{-1}$ and $\alpha = 0.4\times10^{-5}s^{-1}$ cases, whereas for the $\alpha = 1.0\times10^{-5}s^{-1}$ the 179^0 initial phase shift is clearly non-optimal, a smaller initial phase shift would lead to more growth. In part 2, we present a formal method for finding the initial counter shear phase shift which yields maximum growth. Using these methods it can be shown that the 179^0 initial phase shift maximizes streamfunction growth in the $\alpha = 0.4\times10^{-5}s^{-1}$ case.

To summarize, at short non-dimensional wavenumbers the edge waves tend to be advected past each other but as the non-dimensional wavenumber decreases this eventually becomes impossible; ultimately, the edge wave configuration tends toward a 180^0 countershear phase shift.

(c) The streamfunction field.

The streamfunction field is the most important in this model as all other fields depend on it. Here, we detail a specific example of streamfunction growth; *viz*, that corresponding to the $\alpha = 0.4\times10^{-5}s^{-1}$, $2\mu_0$

= 2.1 case discussed above. This case was chosen for detailed examination because it exemplifies rapid growth in significant strain at a wavelength, potentially resolvable by fairly sparse observational networks.

Fig. 8 shows horizontal cross-sections of the perturbation streamfunction wave corresponding to the curve in Fig. 7 for $\alpha = 0.4\times10^{-5}s^{-1}$. The initial amplitude of the wave was chosen to ensure that the root mean square wave slope defined in Part 2 was equal to 0.1. For this wavelength (518 km), the constraint gave an initial amplitude of 0.032 mb. This corresponds to a 0.4 ms^{-1} amplitude in the cross frontal perturbation wind, ($u'_r = -il\Psi'$). This is just 2% of the initial total wind shear across the front (17 ms^{-1}). Over the next 23.5 hr, the streamfunction wave amplifies 27 times to reach the amplitude of 0.85 mb; the wavelength increases to 726.5 km and the perturbation cross frontal wind amplifies 18.4 times to reach the amplitude of 7.4 ms^{-1}. This final value of the across front wind is 30% of the total wind shear across the front at this time (24 ms^{-1}). Despite the fifteen fold amplification in this percentage, the dynamics of the wave remain quasi-linear as the root mean square wave slope only amplifies by a factor of e. This is discussed in more depth in Part 2 of this paper.

Note that in spite of the fact that the countershear phase shift of the edge waves tends to 180^0, (at T'=23.5 hr, the wave depicted in Fig. 8 has $\Delta\chi = 175^0$), the countershear phase shift of the streamfunction wave does not. This is easily explained by noting that the countershear phase shift of the streamfunction wave, $\Delta\chi_\Psi$, may be deduced from (3.13a) to be

$$\Delta\chi_\Psi = \arg^*[-iR\sinh(\mu) - \cosh(\mu)] - \arg^*[iR\sinh(\mu) - \cosh(\mu)].$$

Thus, the difference between $\Delta\chi_\Psi$ and $\Delta\chi$ increases as μ decreases.

(d) Diagnostics for revealing wave structure of observed fronts.

In order to identify frontal waves in data, a suitable diagnostic must be found. Often the first field meteorologists look to is the geopotential or horizontal streamfunction field. Fig. 9 displays this signature for the last 7.8 hrs of development of the wave. Clearly, the details of the waves structure are somewhat obscured by the basic state deformation field and frontal shear. At 15.7 hr, the wave is evident only as a periodic splaying of the streamlines of the total flow. At 19.6 hr and 23.5 hr closed streamlines can be seen but note that the existence of such closed streamlines would probably not be noticed if a larger contour interval had been used. Whether seen or not seen, the existence of such closed contours is important since such low centers might be able to organize convection on the 100-300km scale in such a way that a secondary, diabatically driven development might take place.

The fields in which the basic state has no signature are more likely to give the observationalist a clearer picture of frontal wave structure. Such fields include all along front derivatives of the total wind field. One possibility is $\partial u/\partial y = \partial u_r'/\partial y$. Since $\partial u_r'/\partial y = -l^2\Psi'$, its structure is exactly the same as that shown in Fig. 8. At 23.5 hr its magnitude is $6.4\times10^{-5}s^{-1}$. Another alternative is to examine $\partial v/\partial y = \alpha + \partial v_r'/\partial y$. Horizontal cross sections of the last 7.8 hrs of $\partial v_r'/\partial y$ are shown in Fig. 10. In order to maximize the similarity between these plots and what might be seen in observational data, we plotted these fields on a 50 km grid in the cross front direction. At 15.7 hrs, there is some indication of the structure of this field in region 4. At 19.6 and 23.5 hrs, however, region 4 is not picked up at this resolution. Remarkably, in all these diagrams the $\partial v_r'/\partial y$ field tilts *with* the shear.

To summarize, a method of diagnosing the existence of small amplitude

frontal waves in data is to examine (after having chosen a suitable coordinate frame) the $\partial u/\partial y$ and $\partial v/\partial y$ for wavelike features. A $\partial u/\partial y$ field tilting *against* the shear together with a $\partial v/\partial y$ tilting *with* the shear may be taken as indicative of a frontal wave amplifying by a barotropic process similar to that described here.

5. Concluding remarks.

A semi-analytic description of frontal wave development on an evolving frontal PV strip had been given. The evolution of this frontal vortex strip is that which would arise from a saturated front with nearly parallel M and θ_e surfaces, a barotropic low level layer and an along front wind in close geostrophic balance. These assumptions are supported by observations of fronts in the north-east Atlantic and although they represent a rather severe idealization, we believe that our assumptions yield a description of frontal dynamics as *realistic* as any other analytic model of frontogenesis.

Our description of frontal wave development, which assumes that low-level waves are unaffected by upper level waves, is adequate for investigating the behavior of barotropic waves on an intensifying narrowing PV strip. An aim of future research is to find out how much interactions between upper-level and low-level waves affect barotropic development. Examples of counterpropagating edge wave interactions, where one edge wave propagates on a larger PV gradient than the other shows that when the edge waves move into a growth configuration, the amplitude of the edge wave on the greater PV gradient becomes larger than its counterpart. Such examples, include Eady waves with surface friction, and asymmetric barotropic shear zones such as that corresponding to our cold front. On these grounds, one might expect an analysis of frontal wave growth which included interactions between upper-level and low-level flow to yield growing modes whose

amplitudes were maximized where the PV gradients where maximized, i.e in our model, this occurs at the edges of the low-level barotropic shear zone. This suggests that our model captures the most important dynamical processes affecting frontal waves on an intensifying frontal PV anomaly.

In terms of the normal modes of the stationary states that the evolving front may be thought to pass through, the potential instability of the front increases markedly as the front intensifies. However, because the non-dimensional wavenumber of the front decreases with time, normal mode solutions are not supported by the evolving front. The behavior of the non-modal waves supported by the evolving front are best described in terms of *RT* phase diagrams, which enable the structural development of a wide range of initial states to be inferred at a glance. The *RT* diagrams make it clear how, as a consequence of the decrease of wavenumber with time, a wave, which initially had a wavenumber so high that little growth would come from it in a stationary system, can amplify significantly in the evolving flow because the *RT* vectors associated with it, eventually push it into a configuration ripe for amplification, at a time when the potential instability of the front has increased considerably.

Finally, we note that the structure of a frontal wave is more likely to be extracted from the basic flow in which it is embedded by examining along front derivatives of observed horizontal wind fields. We note that a $\partial u/\partial y$ field tilting *against* the shear together with a $\partial v/\partial y$ field tilting *with* the shear may be taken as indicative of a frontal wave amplifying by a barotropic process similar to that described here.

A limitation of the present analysis is that it is only possible to trace frontal wave development up to the point of frontal collapse. In the atmosphere, discontinuities of the type predicted by the analytic model are

prevented from occurring by some combination of eddy heat and momentum transport. The reason we have chosen not to parameterize these processes in some way to enable our integrations to be extended is that the current model provides an explicit representation of the growth of eddies responsible for horizontal momentum transport. Thus, it is of interest to assess under what conditions these eddies are potentially capable of preventing frontal collapse. This is the main subject of Part 2 of this paper.

Acknowledgements.

In preparing this paper, the authors benefited from discussions with Martin Juckes. One of the authors (Craig Bishop) was financially supported by a Natural Environment Research Council Grant (GR3/6920).

List of selected symbols

α Horizontal deformation or strain rate.

$\bar{u}_a$ Cross front ageostrophic wind of basic state.

$\bar{v}_g$ Thermal wind of basic state, $\bar{v}_{g3}$ and $\bar{v}_{g5}$ denote it in regions 3 and 5.

Z_B Height of barotropic layer

H Height of overlying baroclinic layer. (Rigid lid at Z_B + H).

$\Theta(Z)$ Potential temperature sounding of 12 ^{0}C wet bulb potential temperature moist adiabat.

N^2 Constrains the magnitude of $\partial\bar{\theta}'/\partial Z$; *viz*, $|\partial\bar{\theta}'/\partial Z| \leq (\theta_0/g)N^2$.

(X',Y',Z',T')

Deforming geostrophic coordinates $(X',Y',Z',T')=(Xe^{\alpha T},Ye^{-\alpha T}, Z, T)$

$L,\delta L$ Widths of strip and transition regions in deforming geostrophic coordinates.

$L_c, \delta L_c$

Widths of strip and transition regions in cartesian coordinates.

E_j Equal to $e^{-2\alpha T}(1/f)\partial \bar{v}_g / \partial X$ in region j.

$\bar{\psi}$ Streamfunction for ageostrophic cross-frontal circulation of basic state.

Ψ Streamfunction for total non-divergent horizontal wind field.

Ψ' Streamfunction for perturbation non-divergent horizontal wind field.

$B(X'), F(Z')$

Functions defining horizontal and vertical structure of $\bar{\theta}$.

(u_r, v_r) Total non-divergent horizontal wind field.

(u'_r, v'_r) Perturbation non-divergent horizontal wind field.

$\bar{\zeta}_j$ Absolute vorticity of basic state in region j.

t_c Time at which $\bar{\zeta}_4$ becomes infinite.

T_n Time non-dimensionalised with T_c; $T_n = T'/t_c$.

$\delta\bar{\zeta}_j$ Difference between absolute vorticities of basic state in regions j+1 and j-1; i.e. $\delta\bar{\zeta}_j = \bar{\zeta}_{j+1} - \bar{\zeta}_{aj-1}$.

$\delta\bar{\zeta}_s$ Symmetric part of $\delta\bar{\zeta}_j$ about $X'=0$.

$\delta\bar{\zeta}_n$ Anti-symmetric part of $\delta\bar{\zeta}_j$ about $X'=0$.

$\bar{v}_s$ Symmetric part of $\bar{v}_{gj}\exp(-\alpha T')$ about $X'=0$.

$\bar{v}_n$ Anti-symmetric part of $\bar{v}_{gj}\exp(-\alpha T')$ about $X'=0$.

$\tilde{Q}_j$ Change in perturbation along front wind across transition region j multiplied by $\exp(\alpha T')$.

R Complex parameter governing horizontal structure of waves. $R = (R_r, R_i)$

R_{nm} Value of R which renders $\partial R/\partial T' = 0$; i.e. the normal mode R value.

p' Complex integrated phase speed, $\partial p'/\partial T'$ gives the growth rate and northward propagation rate of the streamfunction wave in deforming coordinates at $X'=0$.

$\Delta\chi$ Countershear phase shift of edge waves.

$\Delta\chi_{nm}$ Countershear phase shift of edge waves in normal mode configuration.

2μ Along front wavenumber multiplied by cartesian width of strip; i.e. the non-dimensional wavenumber.

$2\mu_0$ Initial non-dimensional wavenumber.

l Along front wavenumber in cartesian coordinates

$\overset{*}{l}$ $\overset{*}{l} = 2\mu/L = l_0 e^{-2\alpha T'}(f/\bar{\zeta}_4)$

APPENDIX A: Balance assumption.

It is of interest to assess the accuracy of the assumption of cross-front geostrophic balance in our moist front. Letting $(u, v, \phi) = (-\alpha x + \bar{u}_a, \alpha y + \bar{v}, f\alpha xy - (\alpha^2/2)(x^2 + y^2) + \bar{\phi})$, the inviscid, unapproximated momentum eq. is (cf. Bishop 1993a)

$$D\bar{u}_a/Dt - \alpha\bar{u}_a - f\bar{v} = -\bar{\phi}_x$$

Thus, an appropriate measure of the extent to which the front is out of cross front geostrophic balance is the ratio,

$$\kappa = \left|\left(D\bar{u}_a/Dt - \alpha\bar{u}_a\right)\left(f\bar{v}_g\right)^{-1}\right| = \left|\bar{v}_a/\bar{v}_g\right|$$

where $\bar{v}_a$ denotes the along front ageostrophic wind. Using thermal wind balance in (2.4) and noting that both $\partial\bar{\psi}/\partial Z$ and $\bar{v}_g$ are zero at the height Z_c, it follows that

$$\partial\bar{\psi}/\partial Z = \bar{u}_a + \bar{w}\,(1/f)\partial\bar{v}_g/\partial Z = -\frac{2\alpha}{f}\bar{v}_g. \qquad \text{(A.1)}$$

Hence, in the low level barotropic zone where $\partial\bar{\psi}/\partial Z = \bar{u}_a$ and we may use (A.1) and the along front momentum eq. $(\partial\bar{v}_g/\partial T' = -\alpha\bar{v}_g - f\partial\bar{\psi}/\partial Z')$ to show that

$$D\bar{u}_a/Dt - \alpha\bar{u}_a = \partial\bar{u}_a/\partial T' - \alpha\bar{u}_a = -(2\alpha/f)[\partial\bar{v}_g/\partial T' - \alpha\bar{v}_g]$$
$$= (2\alpha/f)(f\bar{u}_a + 2\alpha\bar{v}_g) = 0.$$

Remarkably, cross-front geostrophic balance is an exact solution to the primitive equations in the barotropic layer. In the non-barotropic regions

of intense highly strained fronts, the balance assumption is less justified. This break down of balance occurs in association with the large vertical velocities[3] arising from our $PV_e = 0$ thermodynamics. Using (A.1), it can be shown that

$$\kappa \cong O\left(\overline{w}\,\frac{\partial\overline{w}}{\partial\overline{Z}'}\frac{\partial\overline{v}_g}{\partial\overline{Z}'}\left(f\overline{v}_g\right)^{-1}\right) \cong O\left(\frac{1}{2}\left(\frac{\overline{\zeta}}{f}\right)^3\left(\frac{\alpha}{f}\right)^2\right)$$

The expression indicates at what point, the predictions of the primitive equations are likely to diverge from those from the balanced equations. This divergence will definitely be significant once κ is order one. For $\alpha/f = 0.1$, this occurs when $\overline{\zeta}/f = 6$. For $\alpha/f = 0.02$, this occurs when $\overline{\zeta}/f = 17$.

APPENDIX B: Algebraic description of the basic state

The basic state is described by the following eq's.

$$\frac{g}{\theta_0}\overline{\theta} = g + \Theta(Z) + \frac{g}{\theta_0}\overline{\theta}'(X',Z',0). \tag{B1}$$

(recall $X'=Xe^{\alpha T}$). Referring to (2.5), which gives $g\overline{\theta}/\theta_0 = F(Z')\left(B(X')-B_0\right)$, the vertical structure function is defined by

$$F(Z') = \begin{cases} 1 + \cos\left\{\dfrac{2\pi}{H}\left[\left(Z'-Z_B\right) - \dfrac{H}{2}\right]\right\} & \text{for } H > Z > Z_B \\ 0 & \text{for } Z_B > Z > 0 \end{cases} \tag{B2}$$

Letting L be the geostrophic coordinate width of region 4 and δL, the corresponding width of the transition regions 3 and 5, the expressions defining $B(X')$ in the seven regions may be written

[3]Since $\partial w/\partial Z = (\overline{\zeta}/f)\partial^2\overline{\psi}/\partial X\partial Z$, (A.1) implies that,

$$\overline{w} = O\left(\frac{\overline{\zeta}}{f}\,\frac{2\alpha}{f}\,\frac{\partial\overline{v}_g}{\partial X}\delta_H\right) = O\left(\frac{\overline{\zeta}}{f}\,\alpha\,\delta_H\right)$$

where δ_H is the height scale over which the vertical velocity changes. Thus, with $\delta_H = 5$ km, and $\alpha = 1\times10^{-5}s^{-1}$, $\overline{\zeta}/f = 6$, it follows that $\overline{w} = O\left(30\text{ cm s}^{-1}\right)$.

$$B(X')=\begin{cases} -\frac{HN^2}{2\pi}+B\left(-\frac{L}{2}-\delta L\right) & \text{for } X'<X_l \\ B\left(-\frac{L}{2}-\delta L\right)+\frac{\partial B}{\partial X'}\left(-\frac{L}{2}-\delta L\right)(Xl)+\frac{A_2}{2}(Xl)^2, & \text{for } X_l\le X'<-\frac{L}{2}-\delta L \\ -\left[\frac{2\Lambda}{L}+A_2\right]\left[\frac{(Xl)^3}{6\delta L}-\frac{\delta L}{2}\left(X'+\frac{L}{2}+\frac{\delta L}{3}\right)\right]+\frac{A_2}{2}\left[X'+\frac{L}{2}\right]^2+\Lambda\left(X'+\frac{L}{4}\right)+\Gamma(Xl), & \text{for } -\frac{L}{2}-\delta L<X'<-\frac{L}{2} \\ -\frac{\Lambda}{L}X'^2+\Gamma(Xl) & \text{for } -\frac{L}{2}\le X'\le\frac{L}{2} \\ \left[\frac{2\Lambda}{L}+A_6\right]\left[\frac{(Xr)^3}{6\delta L}-\frac{\delta L}{2}\left(X'-\frac{L}{2}-\frac{\delta L}{3}\right)\right]+\frac{A_6}{2}\left[X'-\frac{L}{2}\right]^2-\Lambda\left(X'-\frac{L}{4}\right)+\Gamma(Xl), & \text{for } \frac{L}{2}+\delta L>X'>\frac{L}{2} \\ B\left(\frac{L}{2}+\delta L\right)+\frac{\partial B}{\partial X'}\left(\frac{L}{2}+\delta L\right)(Xr)+\frac{A_6}{2}(Xr)^2, & \text{for } X_r\ge X'>\frac{L}{2}+\delta L \\ -\frac{HN^2}{2\pi}+B\left(\frac{L}{2}+\delta L\right) & \text{for } X'>X_r \end{cases} \tag{B3}$$

The coordinates Xl and Xr measure distance relative to the outer edges of regions 3 and 5, respectively; i.e.

$$Xl=X'+\frac{L}{2}+\delta L \text{ and } Xr=X'-\frac{L}{2}-\delta L. \tag{B3b}$$

A consequence of confining temperature gradients to upper levels is that temperature gradients which extend over considerable horizontal distances are associated with large horizontal changes in $\partial\bar{\theta}'/\partial Z'$. Thus, in order to constrain $(g/\theta_0)\left|\partial\bar{\theta}'/\partial Z'\right|$ to always be less than some prescribed parameter, N^2, it is necessary to limit the horizontal extent of regions 2 and 6. This is the role of X_l and X_r in the above equations. They are related to N^2 by the expressions

$$X_l=-\left(\frac{HN^2}{2\pi}\right)\Big/\left\{\frac{1}{2}\left[\frac{\partial B}{\partial X'}\left(-\frac{L}{2}-\delta L\right)\right]\right\}-\frac{L}{2}-\delta L,$$
$$X_r=-\left(\frac{HN^2}{2\pi}\right)\Big/\left\{\frac{1}{2}\left[\frac{\partial B}{\partial X'}\left(\frac{L}{2}+\delta L\right)\right]\right\}+\frac{L}{2}+\delta L. \tag{B3c}$$

The constants A_2 and A_6 define the rate at which $\partial B/\partial X'$ diminishes moving away from region 4. Since $\partial B/\partial X'$ diminishes to zero at X_l and X_r, A_2 and A_6

depend on N^2 and the value of $\partial B/\partial X'$ at the outer edges of regions 3 and 5. To be precise,

$$\frac{A_2}{2} = \frac{1}{4}\left[\frac{\partial B}{\partial X'}\left(-\frac{L}{2}-\delta L\right)\right]^2 \Big/ \left(\frac{HN^2}{2\pi}\right)$$

$$\frac{A_6}{2} = \frac{1}{4}\left[\frac{\partial B}{\partial X'}\left(\frac{L}{2}+\delta L\right)\right]^2 \Big/ \left(\frac{HN^2}{2\pi}\right). \qquad \text{(B3d)}$$

The value of $\partial B/\partial X'$ at the outer edges is determined by solving the quadratics which arise from the requirement that $\partial^2 B/\partial X'^2$ be continuous at $X' = \pm L/2$; (the continuity of $\partial^2 B/\partial X'^2$ at $\pm(L/2 + \delta L)$ is implicitly assured by the form of (B3a)). Assuming that $\Lambda \geq |\Gamma| \geq 0$, and taking the roots of these equations which give positive and negative $\partial B/\partial X'$ at the inner edges of regions 2 and 6, respectively, gives

$$\frac{\partial B}{\partial X'}\left(-\frac{L}{2} - \delta L\right) = \left(\frac{HN^2}{\delta L\pi}\right)\left\{\left\{1 + \frac{2\pi\delta L}{HN^2}\left[\Lambda\left(1 + \frac{\delta L}{L}\right) + \Gamma\right]\right\}^{-1/2} - 1\right\},$$

$$\frac{\partial B}{\partial X'}\left(\frac{L}{2} + \delta L\right) = -\left(\frac{HN^2}{\delta L\pi}\right)\left\{\left\{1 + \frac{2\pi\delta L}{HN^2}\left[\Lambda\left(1 + \frac{\delta L}{L}\right) - \Gamma\right]\right\}^{-1/2} - 1\right\}. \qquad \text{(B3e)}$$

Note that in the limit as δL tends to zero

$$\frac{\partial B}{\partial X'}\left(-\frac{L}{2} - \delta L\right) = \Lambda + \Gamma \text{ whilst } \frac{\partial B}{\partial X'}\left(\frac{L}{2} + \delta L\right) = -\Lambda + \Gamma. \qquad \text{(B4)}$$

Since $\partial^2 \bar{v}_g/\partial X'^2$ is proportional to $\partial^2 B/\partial X'^2$, it follows that the vorticity fields in regions 2, 4 and 6 are proportional to A_2, $-2\Lambda/L$ and A_6, respectively. As indicated by (B3a) and (B4), 2Λ is the amount by which $\partial B/\partial X'$ changes across region 4. The parameter Γ, however, determines the asymmetry in B. For $\Lambda = \Gamma$, $\partial B/\partial X'$ is everywhere greater than zero giving a "pure" cold frontal structure, conversely, with $\Lambda = -\Gamma$, $\partial B/\partial X'$ is less than zero everywhere, giving a "pure" warm frontal structure.

The parameter values common to both the fronts displayed in Fig's 3 and 4 are $\theta_0 = 285.16$ K, $N^2 = 1\times10^{-4}s^{-2}$, $H = 8$ km, $Z_B = 2$ km, $\Lambda = 2.707\times10^{-7}$ s^{-2}, L = 346 km and $T' = 4$ hr/($\alpha\times10^5$s) i.e. both fronts are

displayed at the non-dimensional time $\alpha T' = 0.144$. For the occluded front $\Gamma = 0$, for the cold front $\Gamma = 2.165\times10^{-7}\ s^{-2}$. We took $\delta L = 300$ km and 0 km in Fig's 3 and 4, respectively. The solution to (2.4) may be written in the form

$$\bar{\psi} = -\frac{2\alpha}{f^2} F_{I2}(Z')e^{\alpha T'}\left(\frac{\partial B}{\partial X'}\right)$$

where $F_{I2}(Z')$ is F integrated twice with respect to Z' plus a linear function of Z' which ensures that F_{I2} equals zero at the upper and lower boundaries. Its precise form for $H \geq Z' > Z_B$ is

$$F_{I2}(Z') = \frac{1}{2}\left[Z' - (Z_B + H)\right]\left[(Z' - Z_B) + Z_B\left(\frac{H/Z_B}{1 + H/Z_B}\right)\right] - \left(\frac{H}{2\pi}\right)^2 F(Z') \qquad \text{(B5a)}$$

whilst for $Z_B \geq Z' \geq 0$

$$F_{I2}(Z') = -\frac{H}{2}\left(\frac{H/Z_B}{1 + H/Z_B}\right)Z'. \qquad \text{(B5b)}$$

Numerical analysis of the vertical derivative of $FI2$ shows that $\partial\bar{\psi}/\partial Z'$ is zero at $Z' = Z_c = Z_B + 0.45\ H$. Thus, following the arguments given in section 2, if $\bar{v}_g$ is initially zero at this level it will always be zero at this level. Thus, we integrate the thermal wind relation from this level to obtain,

$$\bar{v}_g(X', Z', T') = e^{\alpha T'}\frac{1}{f}\left(\frac{\partial B}{\partial X'}\right)F_{II}(Z') \qquad \text{(B5a)}$$

where above Z_B

$$F_{II}(Z') = \left[Z' - Z_c\right] + \frac{H}{2\pi}\left\{\sin\left\{\frac{2\pi}{H}\left[\left(Z - Z_B\right) - \frac{H}{2}\right]\right\} - \sin\left\{\frac{2\pi}{H}\left[\left(Z_c - Z_B\right) - \frac{H}{2}\right]\right\}\right\}$$

$$= \left[Z' - Z_c\right] + \frac{H}{2\pi}\left\{\sin\left\{\frac{2\pi}{H}\left[\left(Z - Z_B\right) - \frac{H}{2}\right]\right\} + 0.31153\right\} \qquad \text{(B6b)}$$

whilst below Z_B

$$F_{II}(Z') = F_{II}(Z_B) = -0.4\ H. \qquad \text{(B6c)}$$

The dynamic quantities relevant to the stability analysis presented in Section (3) may now be derived. All these quantities pertain to the flow below Z_B. With $\delta L = 0$, $\bar{v}_g(X', T') = 0$ in regions 1 and 7, whilst

$$\bar{v}_g(X',T') = -e^{\alpha T'}\frac{1}{f}\,0.4\,H\begin{cases}\Lambda + \Gamma + A_2(X' - \frac{L}{2}), & \text{for } X_l \le X' < -\frac{L}{2},\\ -\frac{2\Lambda}{L}X' + \Gamma, & \text{for } -\frac{L}{2} \le X' \le \frac{L}{2},\\ -\Lambda + \Gamma + A(X' + \frac{L}{2}), & \text{for } X \ge X' > \frac{L}{2},\end{cases} \qquad \text{(B7)}$$

The absolute vorticity, $\bar{\zeta}$ (in physical space) is then given by

$$\bar{\zeta}_j = f\left[1 - E_j \exp(2\alpha T')\right]^{-1} \qquad \text{(B9)}$$

where E_j equals E_2, E_4 or E_6 according to the region of interest; i.e.

$$E_j = \begin{cases} E_2, & \text{for } X_l \le X' < -\frac{L}{2},\\ E_4, & \text{for } -\frac{L}{2} \le X' \le \frac{L}{2}\\ E_6, & \text{for } X_r \ge X' > \frac{L}{2},\end{cases} \qquad \text{(B10a)}$$

where

$$E_2 = -\frac{1}{f^2}\,0.4\,\pi\left(\frac{\Gamma + \Lambda}{N}\right)^2,\quad E_4 = \frac{1}{f^2}\,0.4\,H\,\frac{2\Lambda}{L} \text{ and } E_6 = -\frac{1}{f^2}\,0.4\,\pi\left(\frac{\Gamma - \Lambda}{N}\right)^2 \qquad \text{(B10b)}$$

For the above mentioned parameters defining the cold and occluded fronts, E_4 = 0.5. For the occluded front, (the front whose stability we analyse in detail), $E_2 = E_6$ = - 0.092, whilst for the cold front case, E_2 = -0.298 and $E_6 = -3.69\times10^{-3}$.

APPENDIX C. Relationship between $\tilde{Q}_j$'s and streamfunction.

Firstly, note that Green's theorem implies that

$$\int_0^y \left(v'_r(x_b+\delta L_c,\eta) - v'_r(x_b,\eta)\right)d\eta = \int_0^y \int_{x_b}^{x_b+\delta L_c}\left(\frac{\partial^2\Psi'}{\partial x^2} + \frac{\partial^2\Psi'}{\partial y^2}\right)d\mu d\eta + \int_{x_b}^{x_b+\delta L_c}\left(u'_r(\mu,y) - u'_r(\mu,0)\right)d\mu, \qquad \text{(C.1)}$$

where x_b gives the left boundary of the transition region of interest, $(u'_r, v'_r) = (-\partial\Psi'/\partial y,\ \partial\Psi'/\partial x$ and δL_c gives the width of the transition region in Cartesian space. The second term on the right hand side of this equation is negligible provided that

$$(2\pi\delta L_c/\lambda)^2 \le 0.01, \qquad \text{(C.2)}$$

where λ is the along front wavelength. Typically, the fastest growing waves have $\lambda \geq \pi L_c$, where L_c is the width of the vortex strip in physical space; for such waves, the above approximation is satisfied provided that $\delta L/L \leq 0.2f/(\bar{\zeta}+f)$. Taking δL small enough to satisfy (C.2), equation (C.1) becomes, (after differentiating with respect to y),

$$v'_r(x_b+\delta L_c,\ y,\ t) - v'_r(x_b,\ y,\ t) = \int_{x_b}^{x_b+\delta L_c} \zeta'(x,\ y,\ t)\ dx \qquad \text{(C.3)}$$

Since $dx = e^{-\alpha T'} f/\bar{\zeta} dX'$, the deforming geostrophic coordinate counterpart of (C.3) is simply

$$v'_r(-\frac{L}{2}) - v'_r(-\frac{L}{2} - \delta L) = e^{-\alpha T'} \int_{-\frac{L}{2}-\delta L}^{-\frac{L}{2}} Q'(X',\ Y',\ T')dX' = e^{-\alpha T'} \tilde{Q}_3 \qquad \text{(C.4a)}$$

in region 3 and

$$v'_r(\frac{L}{2} + \delta L) - v'_r(\frac{L}{2}) = e^{-\alpha T'} \int_{\frac{L}{2}}^{\frac{L}{2}+\delta L} Q'(X',\ Y',\ T')dX' = e^{-\alpha T'} \tilde{Q}_5 \qquad \text{(C.4b)}$$

in region 5. Thus, the integral of Q' across the transition regions in deforming geostrophic space is $\exp(\alpha T')$ times the difference in perturbation along front velocity across the regions[4].

Appendix D. Definition of arg*.

The arg* function of a complex function of time, $z_{cmp}(t) = (z_r,\ z_i)$ is designed to return the angle between the real axis and z_{cmp}. In addition, however, in order that information concerning the number of times, n, z_{cmp} passes through $\mp\pi$ during a specified time interval be contained in the

[4]If the integral was done with respect to the geostrophic coordinates the exponential term would not appear.

initial value of $\arg^*\left(z_{cmp}(t)\right)$ we define

$$\arg^*\left(z_{cmp}(t)\right) = \pm n\ 2\pi + \tan^{-1}\left(\frac{z_i}{z_r}\right) + \begin{cases} 0 & \text{for any } z_i \text{ and } z_r > 0 \\ -\pi & \text{for } z_i < 0 \text{ and } z_r < 0 \end{cases}$$

where, for example, if the phase of z_{cmp} passed through $-\pi$ twice the first term would be equal to 4π.

REFERENCES

Bishop, C.H., 1993a: On the behaviour of baroclinic waves undergoing horizontal deformation. Part 1: The "RT" phase diagram. *Quart.J.Roy.Meteor.Soc.* 119, 221-240

Bishop, C.H., 1993b: On the behaviour of baroclinic waves undergoing horizontal deformation. Part 2: Error bound amplification and Rossby wave diagnostics. *Quart.J.Roy.Meteor.Soc.* 241-269.

Bretherton, F.P., 1966. Baroclinic instability and the short wave cutoff in terms of potential vorticity. *Quart.J.Roy.Meteor.Soc.* 92,335-345.

Charney,J.G. and Stern.M.E. 1962: On the stability of internal baroclinic jets in a rotating atmosphere. *J.Atmos.Sci.*,19:159-172.

Dritschel, D. G., P.H. Haynes, M.N. Juckes, and T.G. Shepherd, 1991: The stability of a two-dimensional vorticity filament under uniform strain. *J. Fluid Mech.* 230, 647-665.

Eady,E.T. 1949. Long waves and cyclone waves. *Tellus*, 1,33-52.

Emanuel, K.A., 1983: On assessing local conditional instability from atmospheric soundings. *Mon. Wea. Rev.*, 111:2016-2033.

Emanuel, K.A., 1988: Observational evidence of slantwise convective adjustment. *Mon. Wea. Rev.*, 116:1805-1816.

Emanuel, K.A. and A.J. Thorpe, 1985: Frontogenesis in the presence of small

stability to slantwise convection. *J.Atmos.Sci.*,42:1809-1824.

Farrell,B. 1984. Modal and non-modal baroclinic waves. *J.Atmos.Sci.*, 41:668-673.

Hoskins,B.J and Bretherton.F.P. 1972. Atmospheric frontogenesis models: mathematical formulation and solution. *J.Atmos.Sci.*,29:11-37.

Hoskins,B.J., McIntyre,M.E. and Robertson,A.W. 1985. On the use and significance of isentropic potential vorticity maps. *Quart.J.Roy.Meteor.Soc.*, 111, 877-946.

Joly, A. and Thorpe,A.J. 1990: Frontal instability generated by tropospheric potential vorticity anomalies. *Quart.J.Roy.Meteor.Soc.*, 116: 528-560.

Joly, A. and A.J. Thorpe, 1991: The stability of time dependent flows: An application to fronts in developing baroclinic waves. *J.Atmos.Sci.*,48,163-182.

Pedlosky,J. 1964. An initial value problem in the theory of baroclinic instability. *Tellus*, 16:12-17.

Rayleigh, Lord 1880. On the stability, or instability, of certain fluid motions, II, 57-70 (Also in Rayleigh's *Theory of Sound*, Volume 2, § 367, published by Dover.

Thorpe, A.J. and S.A. Clough, 1991: Mesoscale dynamics of cold fronts: Structures described by dropsoundings in Fronts 87. *Quart.J.Roy.Meteor.Soc.*, 117:903-941.

FIGURE CAPTIONS

Fig. 1. Heuristic diagrams of edge wave dynamics. (a) Propagating edge waves on PV strips (shaded). Vectors marked $\bar{v}_g$ indicate cross front shears.

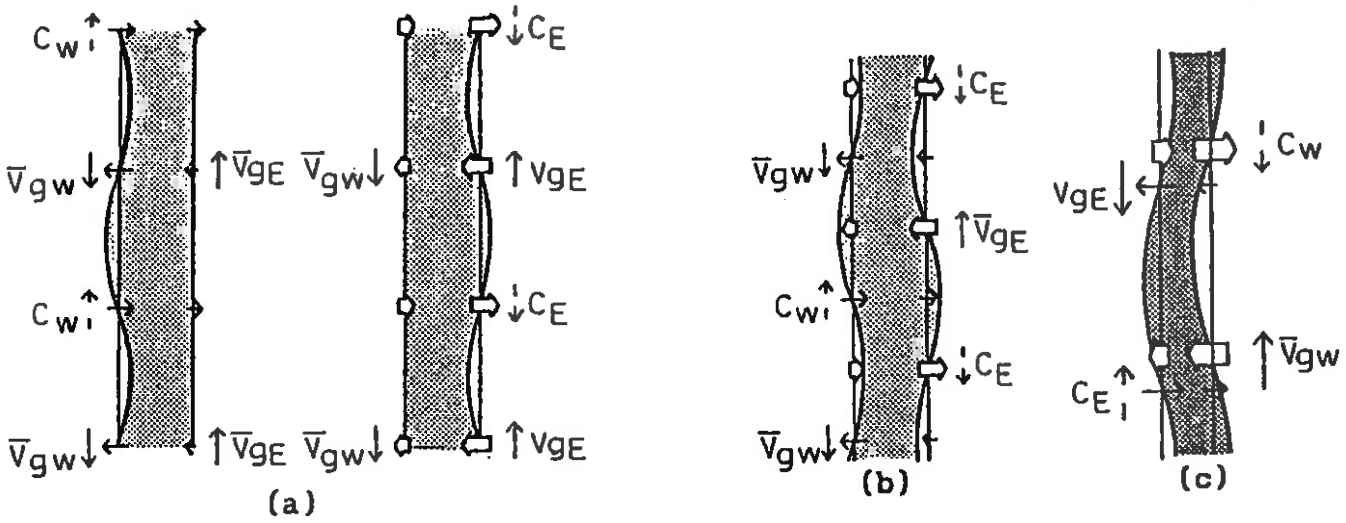

Fig. 1. Heuristic diagrams of edge wave dynamics. (a) Propagating edge waves on PV strips (shaded). Vectors marked $\bar{v}_g$ indicate cross front shears. Broken vectors marked c_W and c_E give propagation velocities of western and eastern edge waves, respectively. Horizontal line and open arrows indicate cross front winds induced by western and eastern edge waves, respectively. (b) Mutually amplifying configuration of eastern and western edge waves. (c) Configuration produced by action of frontogenetic flow on the (b) configuration.

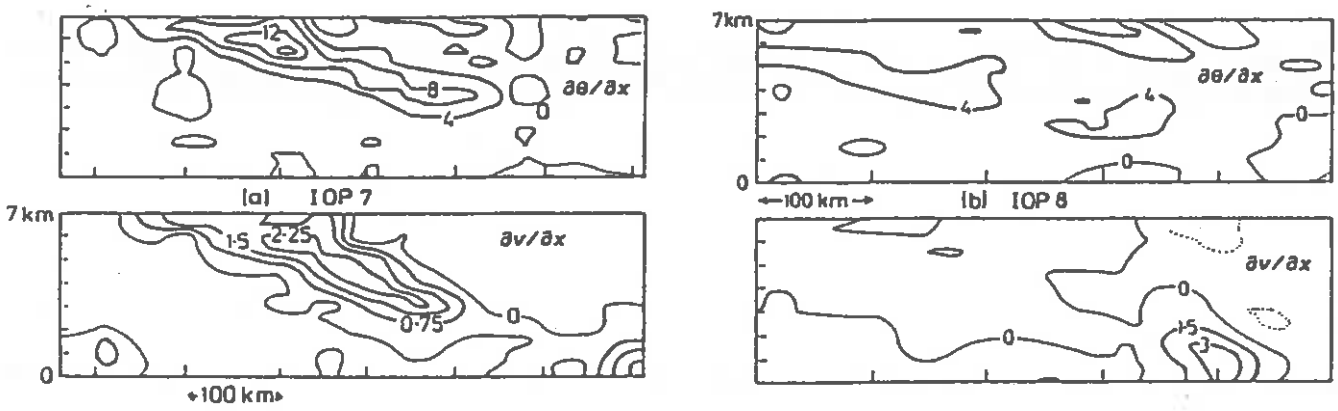

Fig. 2. The cross-frontal temperature gradient, $\partial\theta/\partial x$, and wind shear, $\partial v/\partial x$, from dropsonde data taken in Fronts 87 (for further details of this experiment see Thorpe and Clough 1991).

(a) Run 3 from IOP7; contour intervals are 0.75×10^{-4} s^{-1} for $\partial v/\partial x$ and 4 K $(100\ km)^{-1}$ for $\partial\theta/\partial x$;

(b) Run 3 from IOP8; contour intervals are 1.5×10^{-4} s^{-1} for $\partial v/\partial x$ and 4 K $(100\ km)^{-1}$ for $\partial\theta/\partial x$.

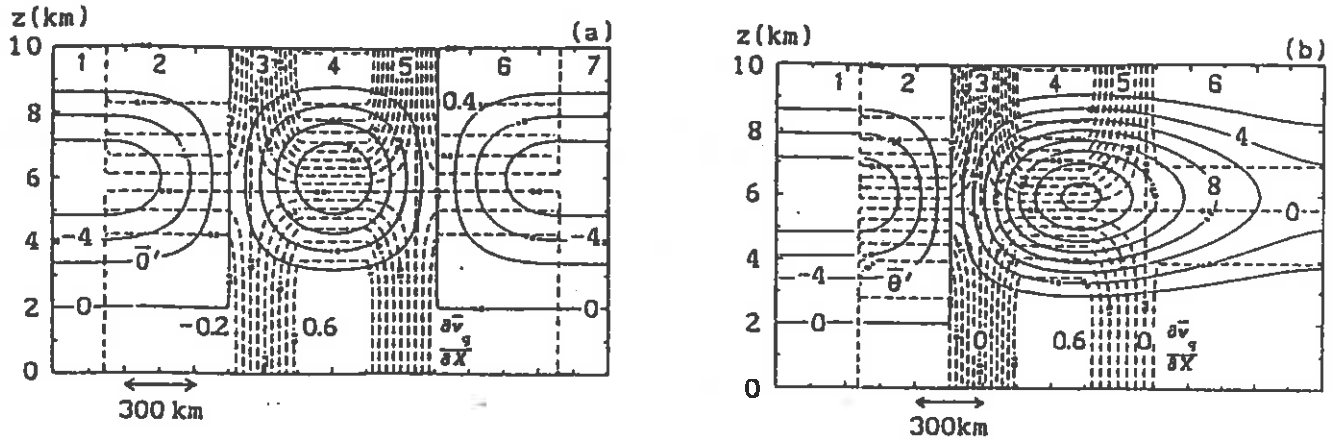

Fig. 3. The seven regions of the idealised front with δL = 300 km at αT = 0.144, depicted in geostrophic (X,Y,Z,T) coordinates: (a) shows the occluded type front (Γ = 0 s^{-2}), (b) the cold front, Γ = $2.165\times10^{-7}s^{-2}$. In both diagrams, dashed lines depict the rate of change of the along front geostrophic with respect to the cross front geostrophic coordinate ($\partial\overline{v}_g/\partial X$) whilst solid lines depict perturbation potential temperature ($g\overline{\theta}'/\theta_0$): contour intervals $0.1\times10^{-4}s^{-1}$ and 2 K, respectively.

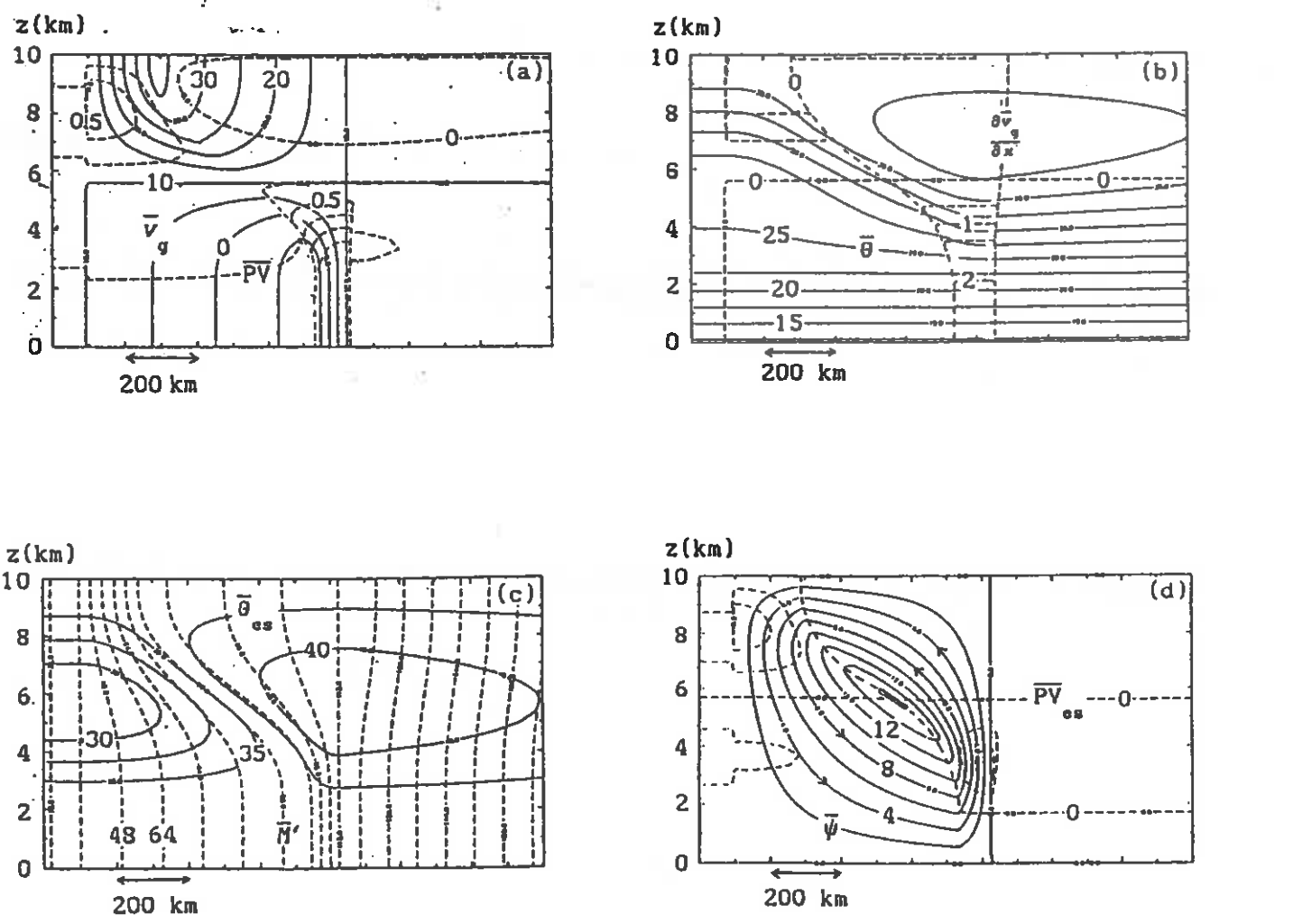

Fig. 4
CAPTION →

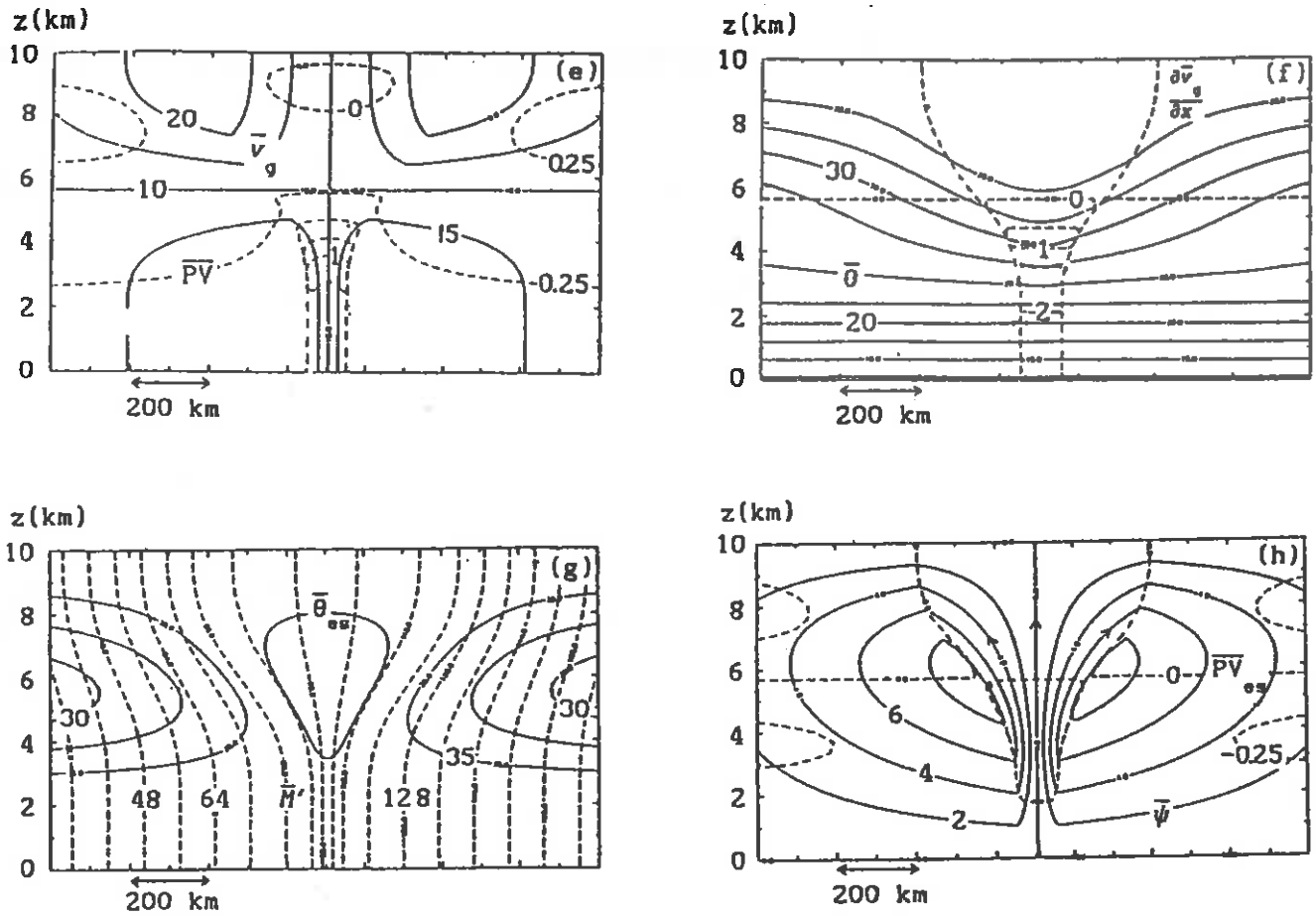

Fig. 4. Examples of the idealized front in physical space. The vertical east-west cross-sections shown have been taken 1000 km north of the center of the deformation field. In (a) - (d) parameters have been chosen so that the structure of the idealized front is similar to that of the IOP7 and IOP8 fronts. Scale analysis suggests that the stability of the low level flow of this idealized front should be similar to that of the occluded type front shown in (e) - (h). For simplicities sake, all the stability calculations of this paper pertain to the occluded type front.

(a) Dashed contours are of $\overline{PV}$ and solid lines give the along front wind; contour intervals are 0.25×10^{-6} $m^2 s^{-1} K(kg)^{-1}$ and 5 ms^{-1}, respectively.

(b) Dashed contours are the vertical component of relative vorticity whilst solid lines describe the potential temperature field; contour intervals $0.5 \times 10^{-4} s^{-1}$ and 2.5 K respectively

(c) Dashed lines show M surfaces whilst solid lines show saturation equivalent potential temperature $\overline{\theta}_{es}$ (in Celsius); contour intervals are 8 ms^{-1} and 2.5 ^{0}C, respectively. Note that in our saturated atmosphere $\overline{\theta}_{es} = \overline{\theta}_{e}$

(d) Dashed lines show $\overline{PV}_{es}$ surfaces $\left(\overline{PV}_{es} = (-\partial \overline{v}_g/\partial z, \vec{\zeta}) \cdot \nabla \overline{\theta}_{es}\right)$ whilst solid lines show streamfunction of cross frontal ageostrophic circulation; contour intervals are 0.25×10^{-6} $m^2 s^{-1} K(kg)^{-1}$ and 2×10^{3} $m^2 s^{-1}$, respectively.

(e) As in Fig. 4(a), but for occluded front.

(f) As in Fig. 4(b), but for occluded front.

(g) As in Fig. 4(c), but for occluded front.

(h) As in Fig. 4(d), but for occluded front.

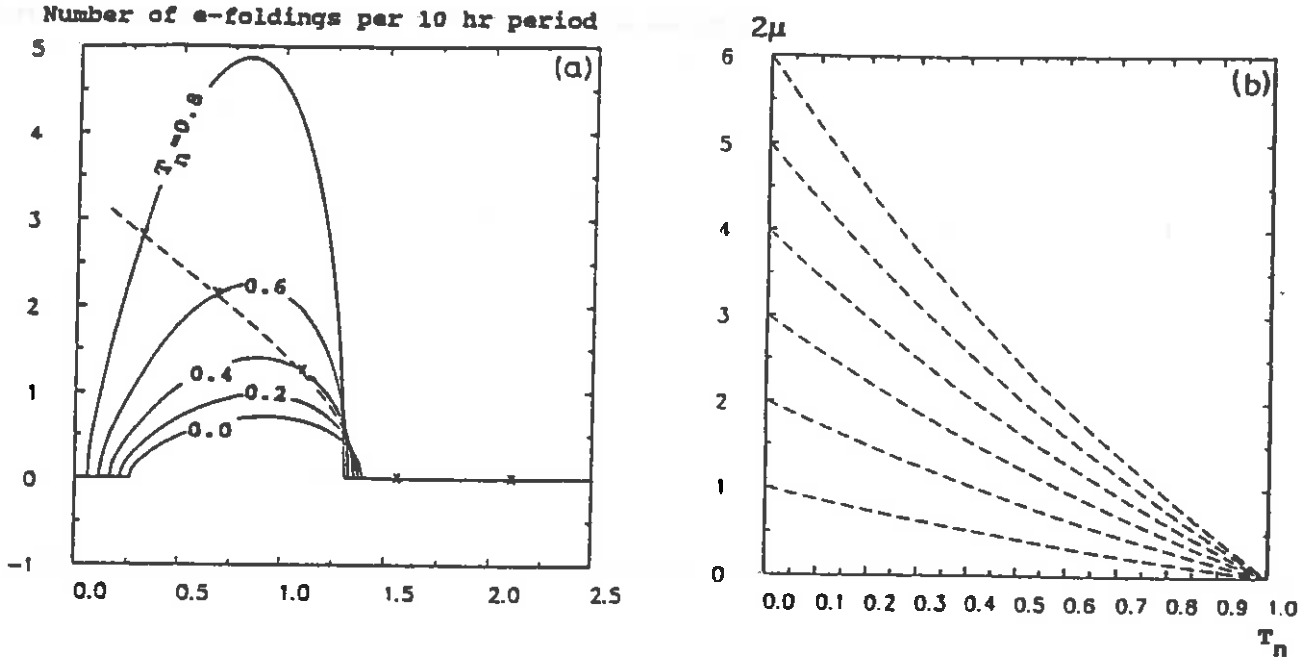

Fig. 5. The variation of "instantaneous" normal mode exponential growth rates with non-dimensional time T_n is depicted by the solid lines in (a). The growth is expressed in terms of the number of e-foldings per 10 hr period. During frontogenesis normal mode growth rates can only be maintained for an instant because the non-dimensional wavenumber of any wave varies with time; the lines in (b), illustrate this variation for a range of initial wavenumbers. The dashed line in (a) shows the growth that a wave which maintained normal mode structure would have as its 2μ value decreased with time from an initial value of 2.1. The passage of time is indicated by the crosses which from right to left mark the 2μ value at T_n = 0, 0.2, 0.4, 0.6 and 0.8.

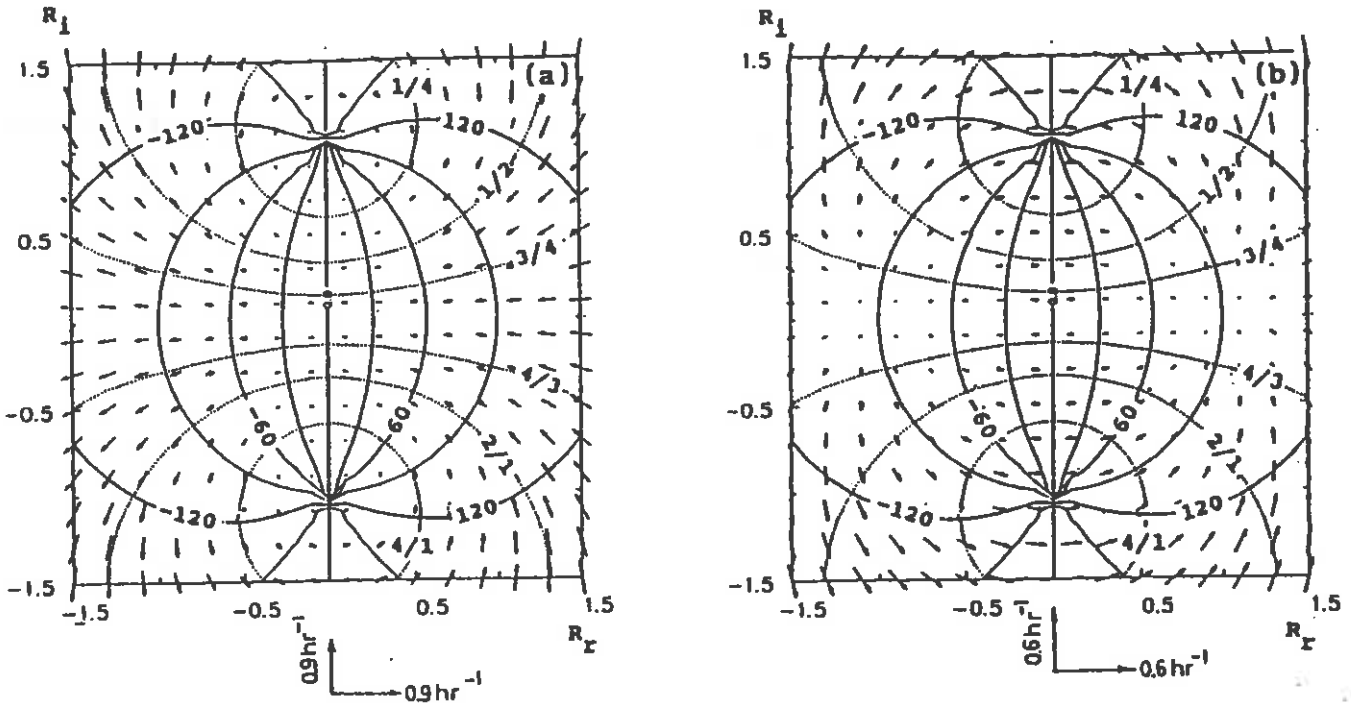

Fig. 6. RT phase diagrams for the cold front. Fig 6(a) pertains to waves with $2\mu = 2.1$ at $T_n = 0$ whilst (b) pertains to waves with $2\mu = 1.083$ and $T_n = 0.4$; (note that all waves which had $2\mu_0 = 2.1$ have $2\mu = 1.083$ at $T_n = 0.4$). The continuous (dashed) lines are contours of positive (negative) $\Delta\chi$ and the contour interval is 30^0. On the R_i axis, $\Delta\chi = 0$ for $|R_i| < 1$ whilst for $|R_i| > 1$, $\Delta\chi = \pm 180^0$. Dotted lines are isolines of $|\tilde{Q}_5|/|\tilde{Q}_3|$. The arrows are proportional to $(\partial R_r/\partial T', \partial R_i/\partial T')$ and are scaled to indicate an "R velocity" in "R units" per hour.

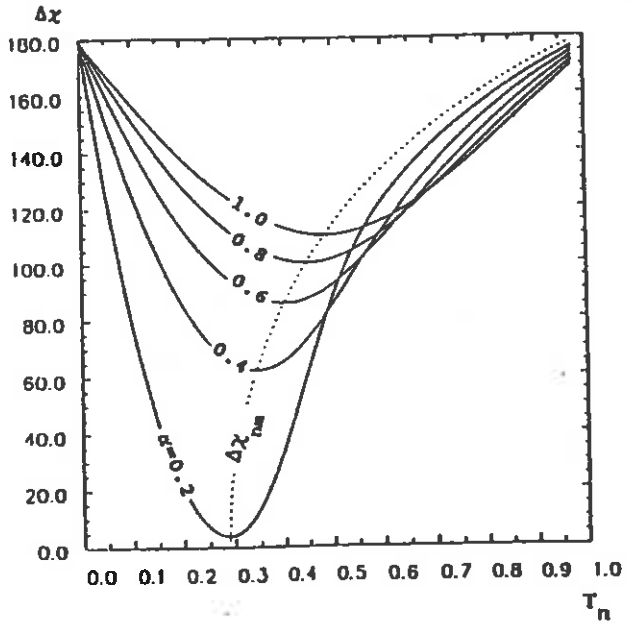

Fig. 7. Variation of $\Delta\chi$ with T_n for wave disturbances with $2\mu_0 = 2.1$ and initial countershear phase shifts of 179^0. This variation depends on the strength of the imposed strain and this is indicated by the solid lines. The strain rates corresponding to each line are indicated in units of $10^{-5}s^{-1}$. The dotted line indicates the variation of $\Delta\chi_{nm}$ with time.

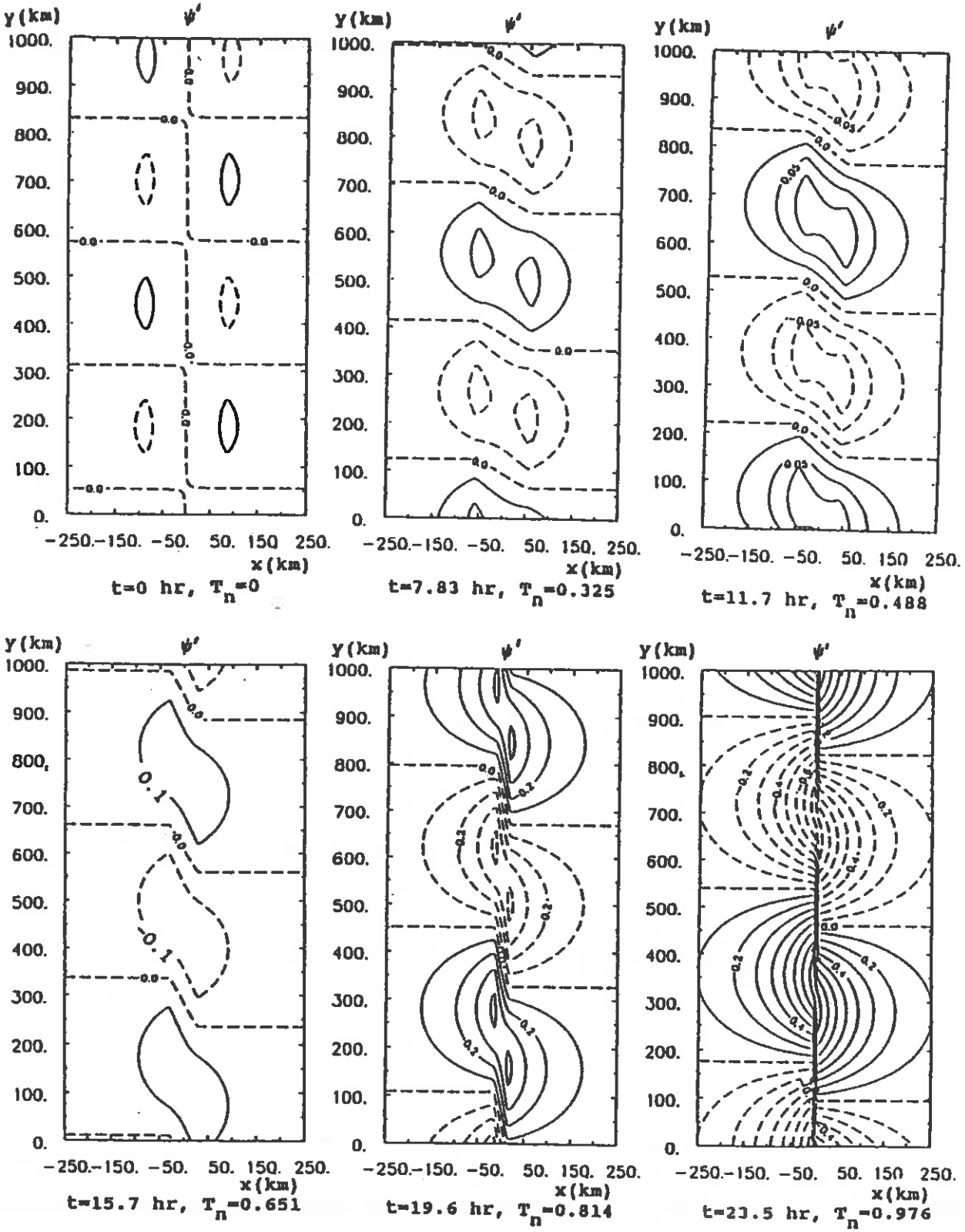

Fig. 8. The evolution of the most rapidly growing streamfunction wave of initial non-dimensional wavenumber 2.1 on a front developing in a strain field with an along front stretching rate of $0.4\times10^{-5}s^{-1}$. The field shown is the perturbation streamfunction converted to pressure units of hectopascals so that, if the flow were geostrophic, its surface perturbation pressure field would be as depicted. Negative contours are dashed. From t = 0 hr to t = 11.7 hr the contour interval is 0.025 mb; thereafter it is 0.1 mb.

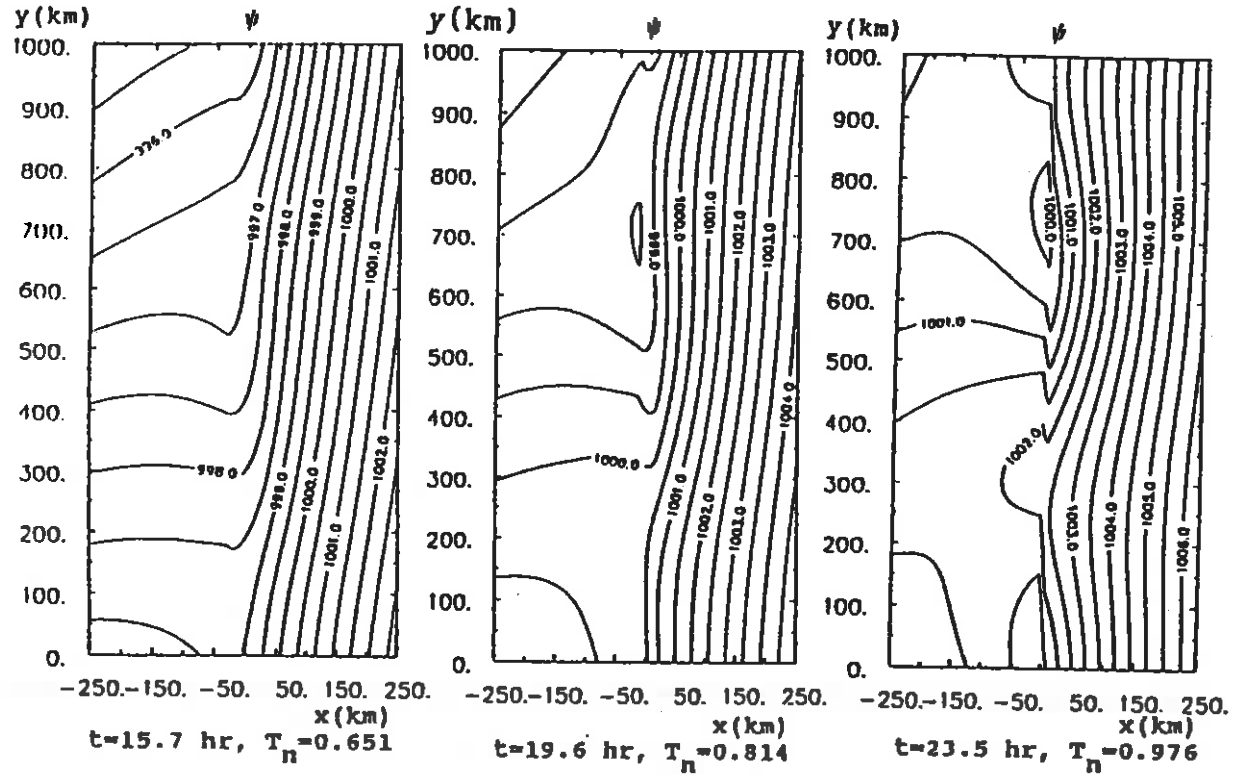

Fig. 9 As in 8, but here the structure of the total streamfunction is indicated. The contour interval is 0.5 mb. The initial position of the front was assumed to be 1000 km to the west of the center of the deformation field. The windows shown above move eastwards with the front as it is advected eastwards by the deformation field and show only that section of the front 1500 km to 2500 km north of the axis of contraction. Only the last 7.8 hr of development are shown as the wave is barely perceptible in the total streamfunction field at earlier times.

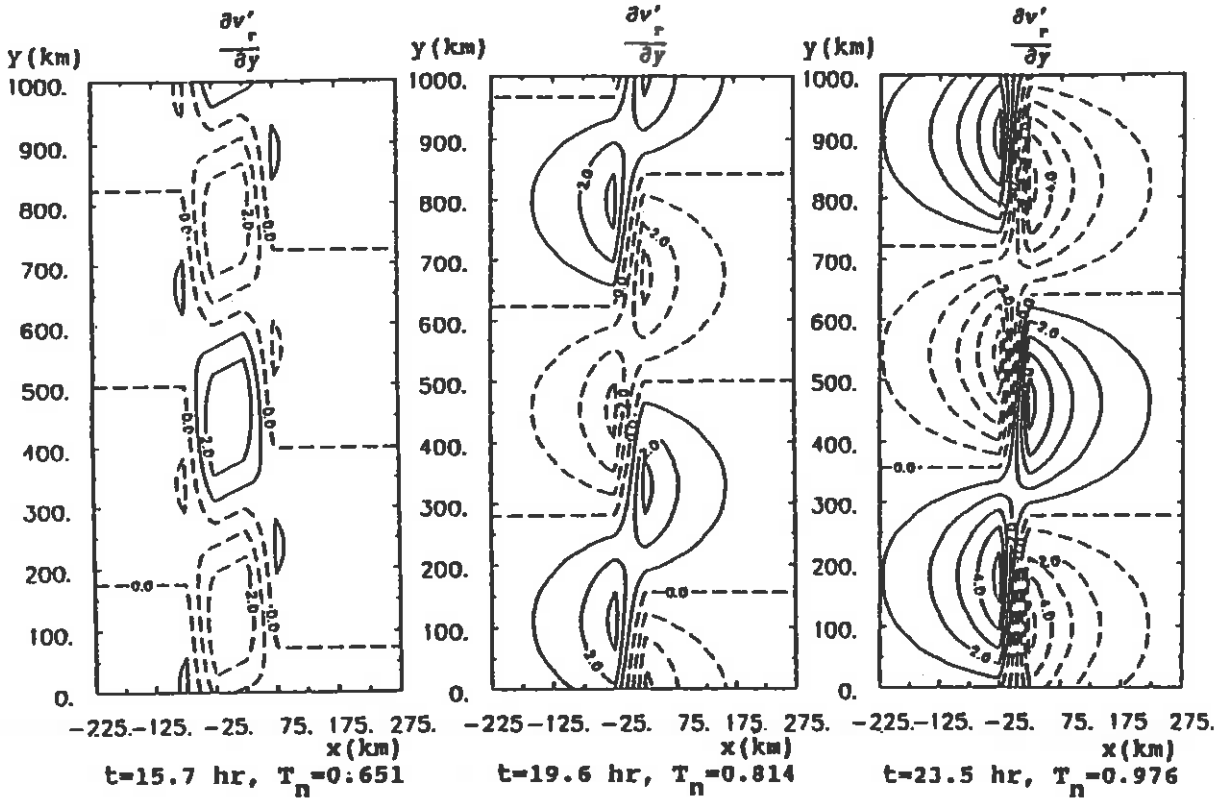

Fig. 10. As in 8, but here $\partial v'_r/\partial y$ is plotted and only the last 7.8 hrs of development are shown. The contour interval is $1\times10^{-5}s^{-1}$.

CURRENT JCMM INTERNAL REPORTS

This series of JCMM Internal Reports, initiated in 1993, contains unpublished reports and also versions of articles submitted for publication. The complete set of Internal Reports is available from the National Meteorological Library on loan, if required.

1. **Research Strategy and Programme.**
   K A Browning et al
   January 1993

2. **The GEWEX Cloud System Study (GCSS).**
   GEWEX Cloud System Science Team
   January 1993

3. **Evolution of a mesoscale upper tropospheric vorticity maximum and comma cloud from a cloud-free two-dimensional potential vorticity anomaly.**
   K A Browning
   January 1993

4. **The Global Energy and Water Cycle**
   K A Browning
   July 1993

5. **Structure of a midlatitude cyclone before occlusion.**
   K A Browning and N Roberts
   July 1993

6. **Developments in Systems and Tools for Weather Forecasting.**
   K A Browning and G Szejwach
   July 1993

7. **Diagnostic study of a narrow cold frontal rainband and severe winds associated with a stratospheric intrusion.**
   K A Browning and R Reynolds
   August 1993

8. **Survey of perceived priority issues in the parametrizations of cloud-related processes in GCMs.**
   K A Browning
   September 1993

9. **The Effect of Rain on Longwave Radiation.**
   I Dharssi
   September 1993

10. **Cloud Microphysical Processes - A Description of the Parametrization used in the Large Eddy Model.**
    H Swann
    October 1993

11. **An Appreciation of the Meteorological Research of Ernst Kleinschmidt.**
A J Thorpe
May 1992

12. **Potential Vorticity of Flow Along the Alps.**
A J Thorpe, H Volkert and Dietrich Heimann
August 1992

13. **The Representation of Fronts.**
A J Thorpe
January 1993

14. **A Parametrization Scheme for Symmetric Instability: Tests for an Idealised Flow.**
C S Chan and A J Thorpe
February 1993

15. **The Fronts 92 Experiment: a Quicklook Atlas.**
Edited by T D Hewson
November 1993

16. **Frontal wave stability during moist deformation frontogenesis.**
Part 1. Linear wave dynamics.
C H Bishop and A J Thorpe
May 1993

Met Office Joint Centre for Mesoscale Meteorology Department of Meteorology
University of Reading PO Box 243 Reading RG6 6BB United Kingdom
Tel: +44 (0)118 931 8425 Fax: +44 (0)118 931 8791
www.metoffice.com